




RESEARCH ARTICLE

Upper-tropospheric inflow layers in tropical cyclones

Shanghong Wang¹  | Roger K. Smith¹  | Michael T. Montgomery² 

¹Meteorological Institute, Ludwig Maximilians University of Munich, Munich, Germany

²Department of Meteorology, Naval Postgraduate School, Monterey, California

Correspondence

R.K. Smith, Meteorological Institute, Ludwig-Maximilians University of Munich, Theresienstrasse 37, 80333 Munich, Germany.
Email: roger.smith@lmu.de

Funding information

National Science Foundation Office of Naval Research, Grant/Award Numbers: AGS-1313948, IAA-1656075, N0001420WX01473

Abstract

Three-dimensional numerical simulations of tropical cyclone intensification with sufficient vertical resolution have shown the development of a layer of strong inflow just beneath the upper-tropospheric outflow layer as well as, in some cases, a shallower layer of weaker inflow above the outflow layer. Here we provide an explanation for these inflow layers in the context of the prototype problem for tropical cyclone intensification, which considers the evolution of a vortex on an f -plane in a quiescent environment, starting from an initially symmetric, moist, cloud-free vortex over a warm ocean. We attribute the inflow layers to a subgradient radial force that exists through much of the upper troposphere beyond a certain radius. An alternative explanation that invokes classical axisymmetric balance theory is found to be problematic. We review evidence for the existence of such inflow layers in recent observations. Some effects of the inflow layers on the storm structure are discussed.

KEYWORDS

hurricane, tropical cyclone, typhoon, vortex intensification

1 | INTRODUCTION

The last few years have seen the possible importance of the outflow layer in tropical cyclone behaviour brought to the fore (e.g., Rappin *et al.*, 2011; Emanuel, 2012; Doyle *et al.*, 2017; Komaromi and Doyle, 2017; Tao *et al.*, 2019). Rappin *et al.* (2011) claimed to have demonstrated that “weak inertial stability in the outflow layer minimizes an energy sink of the tropical cyclone secondary circulation and leads to more rapid intensification to the maximum potential intensity”. However, in many simulations of tropical cyclone behaviour, including the one to be described here, the outflow becomes primarily a region of *inertial instability* (e.g., Smith *et al.*, 2018a) so that, as shown here

in Sections 5 and 6, ideas based on balance arguments are questionable.

Emanuel (2012) hypothesized that tropical cyclone intensification is controlled by small-scale turbulent mixing in the upper-tropospheric outflow and offered an analytical theory in which a parametrization of this mixing process is the sole positive term in an equation for the tendency of the maximum tangential wind (his equation (16)). Nevertheless, the physics of the intensification process, i.e., how in reality this mixing would lead to the required inward movement of the surfaces of absolute angular momentum at low levels for spin-up, remain to be articulated (Montgomery *et al.*, 2019; Montgomery and Smith, 2019).

The presumed importance of the outflow layer in the intensification process motivated a recent field experiment conducted in the Atlantic and Eastern Pacific sectors, called the Tropical Cyclone Intensity (TCI) experiment (Doyle *et al.*, 2017). The main motivation for this experiment appears to rest on the overarching hypothesis that “this upper-tropospheric layer is a critical one, as changes in the TC (tropical cyclone, our insertion) outflow can directly *cause* (our emphasis) changes in the TC secondary circulation” (Doyle *et al.*, 2017, p. 2113). “The overarching goal of the TCI programme is to improve the prediction of TC intensity change, especially rapid intensification (RI) and rapid decay (RD), as well as TC structural changes that are hypothesized to occur through synergistic interaction with outflow” (Doyle *et al.*, 2017, p. 2114).

The researchers of the TCI programme listed several key science goals to address as part of their programme. Two of them stand out as particularly important (Doyle *et al.*, 2017, p. 2114):

- To understand the coupling of tropical cyclone outflow with inner-core convection and its implications for intensity change;
- To interpret observations of the fine-scale horizontal and vertical structure of the outflow layer and inner-core regions of the tropical cyclone.

Most notably, there was no mention of the possible existence and role of upper-tropospheric inflow layers that are found to develop in numerous numerical model simulations of tropical cyclone intensification where the vertical resolution is sufficient (e.g., Rotunno and Emanuel 1987, figure 5c; Hausman *et al.*, 2006, figures 4b and 8b; Bui *et al.*, 2009, figure 6a; Persing *et al.*, 2013, figures 15a, 17a, and 18a; Bu *et al.*, 2014, figures 4a,b, 9a,b, 12, and 16; Smith *et al.*, 2014, figure 2c; Ohno and Satoh 2015, figure 2b; Fovell *et al.*, 2016, figures 11–21; Kieu *et al.*, 2016, figures 2b and 4; Heng *et al.*, 2017, figure 4c; Chen *et al.*, 2018, figure 14a,c; Smith *et al.*, 2018b, figure 2b,d). Most of these papers relate to the evolution of a tropical-cyclone-like vortex in the prototype problem for tropical cyclone intensification, which considers the evolution of a vortex on an f -plane in a quiescent environment, starting from an initially symmetric, moist, cloud-free vortex over a warm ocean. Some of the studies show inflow layers above and below the outflow layer, while others focus on the layer above the outflow layer in the lower stratosphere.

Only recently have detailed observations of the tropical cyclone outflow layer become available, largely as a result of the use of unmanned aircraft drones to release dropwindsondes into storms from the lower stratosphere (e.g., Braun *et al.*, 2016). While the main purpose of such measurements was to document the outflow layer itself,

the data offer the opportunity to detect any layers of inflow in the vicinity of the outflow layer. A comprehensive study of such dropsonde data was presented by Komaromi and Doyle (2017) and Duran and Molinari (2018). These analyses, together with one of *Hurricane Edouard* (2013) by Smith *et al.* (2019), do point to the existence of a layer of enhanced inflow above and/or below the outflow in nature (Section 4). The possible importance of these inflow layers and their role in storm behaviour would seem to merit further study.

At an early stage of the present investigation, a possible explanation for the inflow layers seemed to be an extension of the result of Shapiro and Willoughby (1982) that, if the tangential flow is in thermal wind balance, the response of the secondary circulation to a point source of positive tangential momentum is an outward flow through the source and a compensating inward flow above and below it. Such an explanation is explored in Section 5, where it is shown to be problematic.

As far as we are aware, a satisfactory explanation for these layers and their possible significance for the storm itself, has not been provided. Zhang and Chen (2012) and Chen and Zhang (2013) drew attention to the inflow layer above the upper-tropospheric outflow layer, attributing this layer to the detrainment of deep “convective bursts” in the developing eyewall region. However, these studies fell short of investigating the forces responsible for the inflow layer (an appraisal of these papers was provided by Smith and Montgomery 2015). Kieu *et al.* (2016) found upper-level inflow layers in the lower stratosphere as part of their examination of so-called double warm-core structures in intense tropical cyclones. An appraisal of their explanation for this upper-level inflow layer, is given in Appendix A. Like the Zhang and Chen studies, this explanation falls short of investigating the forces responsible for the inflow layer.

Referring to the results of Bu *et al.* (2014) and Fovell *et al.* (2016), Duran and Molinari (2019) inferred that cloud-top cooling modifies the circulation near the cloud top, driving a weak inflow above the cooling maximum and outflow below, along with subsidence within the region of cooling. However, this is at best a partial explanation because a change in radial flow requires a net force field in the radial direction, the origin and nature of which were not discussed.

A recent analysis of the mean and eddy contributions to tropical cyclone spin-up in an idealized, high-resolution, numerical simulation of tropical cyclone intensification by Montgomery *et al.* (2020) pointed to an alternative explanation for the upper-tropospheric inflow layers. They suggested that these layers are primarily a result of a negative agradient force field that develops in the upper troposphere, apparently as a response to the

outflow itself. As their study was focussed largely on the vortex spin-up at low levels and in the eyewall, the vertical resolution of the model was largest in the boundary layer. The present paper focusses on the evolution and three-dimensional structure of the upper-tropospheric inflow layers using a modified version of the model used by Montgomery *et al.* (described in Section 2) with increased vertical resolution in the upper troposphere and reduced vertical resolution at low levels. In addition, because it concentrates on the upper troposphere, the new simulation includes a representation of cloud microphysics, unlike that of Montgomery *et al.*

The results of the new simulation and related interpretations are presented in Section 3. Section 4 summarizes recent observational analyses of storm structure that show upper-tropospheric inflow layers, while Section 5 examines issues with an interpretation of the inflow layers on the basis of traditional axisymmetric balance theory. Section 6 shows diagnostics of normalized agradient force, a measure of the degree of imbalance in the numerical simulation. The conclusions are presented in Section 7.

2 | THE NUMERICAL MODEL

The calculations presented here are carried out using the latest version of the three-dimensional, non-hydrostatic, numerical cloud model CM1 (cm1r19.8). The horizontal domain is $2,940 \times 2,940$ km in size with 960 grid points in each direction. A horizontal grid spacing of 1 km is used in a central domain 600×600 km. Outside this domain, the grid spacing is stretched uniformly from 1 to 12 km. There are 78 vertical levels from 0 to 25 km. The vertical grid spacing is 100 m in the first 1 km and 500 m from 16 to 25 km. Between 1 and 16 km, the vertical grid spacing is stretched smoothly from 100 to 500 m.

The initial condition is a prescribed, warm-cored, axisymmetric vortex in thermal wind balance in an otherwise quiescent environment. The initial vortex has a maximum tangential wind speed of $15 \text{ m}\cdot\text{s}^{-1}$ at the surface at a radius of 100 km. The tangential wind decreases sinusoidally with height to zero at 20 km and is set to zero above this altitude. The corresponding balanced pressure, density and temperature fields are obtained using the method of Smith (2006).

The physical parametrization schemes include the Morrison double-moment microphysics scheme (Bryan and Morrison, 2012), a simple planetary boundary-layer parametrization (Bryan and Rotunno, 2009) and, because of the comparatively short duration of the integrations, no thermal radiation scheme. Instead, a Newtonian relaxation to the temperature field is used with a time-scale of

10 days instead of the 12 hr default value (footnote 1 of Montgomery *et al.*, 2020).

Rayleigh damping layers with an e-folding time-scale of 5 min are implemented to suppress the reflection of internal gravity waves. These layers are above 20 km height and within 100 km of the open-radiative lateral boundaries. The Coriolis parameter f is set to a constant value of $0.5 \times 10^{-4} \cdot \text{s}^{-1}$, corresponding with a latitude of approximately 20°N . The sea surface temperature is taken to be constant and equal to 27°C . The Dunion moist tropical sounding (Dunion, 2011) is used to characterize the background thermodynamic state. As in Persing *et al.* (2013), the horizontal and vertical mixing lengths are set as 700 and 50 m, respectively, and are assumed constant in both space and time. These values are close to those recommended by Bryan (2012) in order to produce realistic hurricane structure. Montgomery *et al.* (2019) provide further detailed justification for these selected parameter values.

Model output data are stored every 15 min during the simulation for a total period of 90 hr. For certain time periods (41–43 hr, 59–61 hr, 73–75 hr), data were output at 1 min intervals to facilitate accurate tendency calculations and supporting interpretations.

3 | RESULTS

3.1 | Vortex evolution

Figure 1a shows the time evolution of the maximum azimuthally averaged¹ tangential wind speed, V_{max} , and maximum total wind speed, VT_{max} , in the simulation. The determination of centre location for the azimuthal average is described in Appendix B. The green dashed line in Figure 1a shows the threshold slope for rapid intensification (RI), which is defined as a rate of at least $15 \text{ m}\cdot\text{s}^{-1}\cdot\text{day}^{-1}$. With this definition, the vortex enters an RI stage at about 30 hr, a stage that lasts until about 65 hr. Thereafter, the vortex as characterized by V_{max} enters a quasi-steady mature phase until the simulation is terminated at 90 hr. The mature intensity measured by V_{max} is about $75 \text{ m}\cdot\text{s}^{-1}$. As in many previous studies (e.g., Nguyen *et al.*, 2008), VT_{max} is typically between 5 and $10 \text{ m}\cdot\text{s}^{-1}$ larger than V_{max} , a reflection of localized deep convection that first begins to form at about 5 hr.

The time evolution of the maximum azimuthally averaged radial wind speed in different vertical layers is shown

¹The azimuthal average of a quantity α is defined by

$$\bar{\alpha} = \frac{1}{2\pi} \int_0^{2\pi} \alpha d\lambda,$$

where λ is the azimuthal angle.

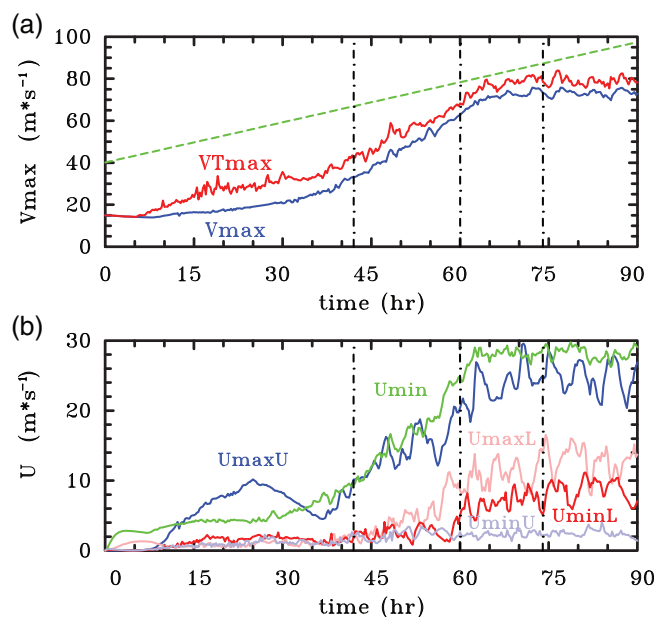


FIGURE 1 Time evolution based on 15 min output of (a) the maximum azimuthally averaged tangential wind speed (V_{max} , blue) and maximum total wind speed (VT_{max} , red) and (b) the magnitude of the maximum azimuthally averaged radial wind speed in different layers: boundary-layer inflow (U_{min} , green), upper-tropospheric outflow (U_{maxU} , blue), boundary-layer outflow (U_{maxL} , pink), inflow beneath the upper-level outflow (U_{minL} , red), inflow above the upper-level outflow (U_{minU} , light blue). The green dashed line in (a) indicates a slope corresponding to the normal definition of RI ($15 m \cdot s^{-1} \cdot day^{-1}$). Vertical dashed lines indicate the times which are discussed in the text. The precise layers for radial velocity extrema are: U_{min} and U_{maxL} , 0–3 km; U_{minL} , 8–13 km; U_{maxU} , 10–16 km; U_{minU} , 13–18 km.

in Figure 1b. The maximum radial inflow in the boundary layer², U_{min} , has a similar behaviour to V_{max} . It increases steadily from about 30 hr, reaches a maximum magnitude at the beginning of the mature stage and subsequently levels off. Typically, U_{min} is less than 40% of V_{max} .

The maximum outflow just above the top of the boundary-layer inflow layer, U_{maxL} , begins to increase in a time-mean sense after about 45 hr and levels off during the mature stage, but it has much larger fluctuations than the maximum inflow beneath the upper-level outflow, U_{minL} , beyond 54 hr.

The maximum in the upper-layer outflow, U_{maxU} , has a peak near 25 hr, followed by a decline to 37 hr, just after the start of RI. This peak is associated with an early episode of some individual deep convection cells. Subsequently, U_{maxU} increases rapidly throughout the RI phase, but levels off in a time-mean sense after about

65 hr. Nevertheless, like U_{maxL} , it fluctuates markedly after about 48 hr.

The maximum inflow immediately below the upper-layer outflow strengthens in a time-mean sense from about 58 hr, reaches a peak at about 82 hr, after which it declines a little. Moreover, like U_{maxL} and U_{maxU} , it exhibits significant fluctuations.

The maximum inflow immediately above the main upper-level outflow layer, U_{minU} , increases slightly from near the start of the RI period, but remains less than about $2.5 m \cdot s^{-1}$. Its behaviour does not appear to have a strong connection with other metrics of vortex development.

3.2 | Azimuthally averaged vertical structure

Figures 2a, c, e show the azimuthally and 1 hr time-averaged tangential velocity, \bar{v} , at selected times with the corresponding surfaces of absolute angular momentum, $\bar{M} = r\bar{v} + (1/2)fr^2$, superimposed. Here f is the Coriolis parameter and r is the radius. Figure 2a is for 42 hr, a few hours after the RI period commences, Figure 2c is for 60 hr, a few hours before the quasi-steady period is reached, and Figure 2e is for 74 hr, which is in the middle of the quasi-steady period. Figures 2b, d, f show the corresponding similarly averaged radial velocity, \bar{u} , with selected contours of vertical velocity superimposed.

The tangential velocity fields have similar characteristics to those described in many previous studies, the maximum occurring at a low altitude near the top of a shallow layer of strong inflow adjacent to the sea surface and well within a radius of 50 km. At radii larger than about 75 km at 42 and 60 hr, the maximum tangential wind occurs in the low to middle troposphere, at least to about 250 km radius, a feature evidenced most clearly by the location of the inward-pointing nose of the \bar{M} -surfaces in this region. At 74 hr, the middle tropospheric maximum extends only to about 160 km radius.

Invoking the classical paradigm for tropical cyclone intensification that is based on the approximate material conservation of absolute angular momentum above the frictional boundary layer (Montgomery and Smith 2014; Montgomery and Smith 2017), this maximum must be associated with a relatively strong time-mean inflow at this level. A notable feature of the \bar{M} -surfaces at all times shown is their quasi-horizontal orientation in the vicinity of the upper-tropospheric outflow with a propensity to fold over in this region. At large radii in the region of outflow, typically larger than 200 km at the later times, the tangential flow becomes anticyclonic, a well-known feature that, again, is a consequence of the approximate conservation of absolute angular momentum in the outflow.

²Here, we refer to the boundary layer as the layer adjacent to the surface, typically 1 km deep, where the radial inflow exceeds $2 m \cdot s^{-1}$.

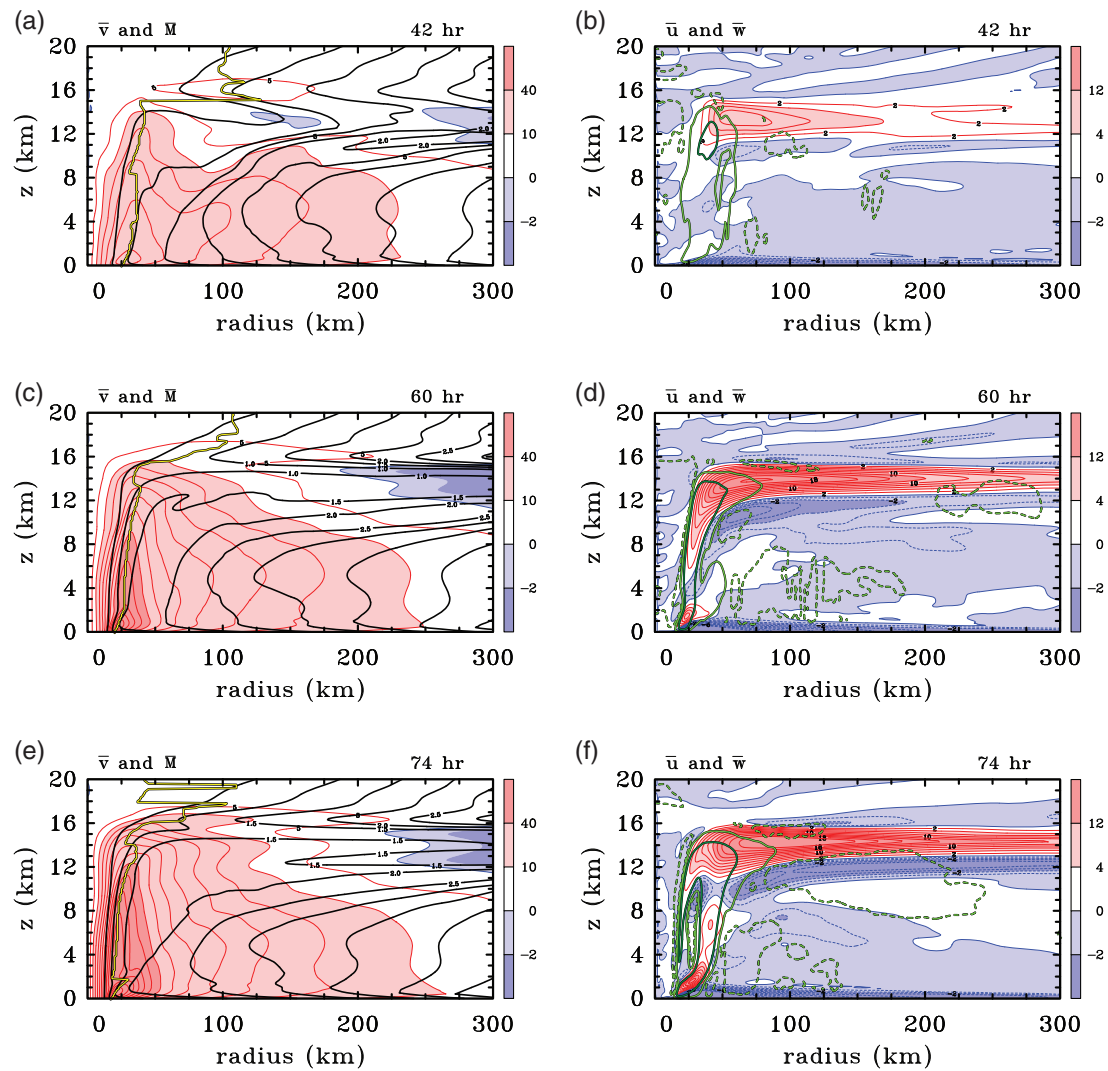


FIGURE 2 Radius–height cross sections of 1 hr time-averaged (based on 1 min output) and azimuthally averaged fields from the numerical model simulation at (a, b) 42 hr, (c, d) 60 hr and (e, f) 74 hr. (a, c, e) show tangential velocity component, \bar{v} (shaded contours, interval $5 \text{ m}\cdot\text{s}^{-1}$) and surfaces of absolute angular momentum, \bar{M} (black contours, interval $0.5 \times 10^6 \text{ m}^2\cdot\text{s}^{-1}$). (b, d, f) show the radial velocity component, \bar{u} (shaded contours with interval $2 \text{ m}\cdot\text{s}^{-1}$ when $\bar{u} > 0$, and $1 \text{ m}\cdot\text{s}^{-1}$ when $\bar{u} < 0$) and vertical velocity component, \bar{w} (three green contours at $+0.25 \text{ m}\cdot\text{s}^{-1}$ (solid light), $+1.0 \text{ m}\cdot\text{s}^{-1}$ (solid dark) and $-0.02 \text{ m}\cdot\text{s}^{-1}$ (dashed)). Red solid contours indicate positive values, and blue dashed contours negative values. The yellow curve indicates the radius of maximum tangential wind at each height

The radius of maximum tangential wind generally increases with height in the low to middle troposphere as shown by the yellow curve in Figures 2a,c,e, although at 74 hr (e), there is a sharp decrease in radius marking a second wind maximum in the eyewall updraught complex. This maximum is an indication of a quasi-stationary centrifugal wave generated by the recoil of the shallow outflow just above where the boundary layer terminates (e.g., Montgomery and Smith 2017; Stern *et al.*, 2020).

Figures 2b,d,f show the evolution of the radial flow between 42 and 74 hr. The prime focus here is on the development of the upper-level outflow and the layers of inflow above and below it. At 42 hr, the outflow layer resides between about 11–15 km height near its source, just inside

a radius of 40 km, and it tapers slightly with increasing radius. The maximum velocity in the outflow layer at this stage is about $9.6 \text{ m}\cdot\text{s}^{-1}$. There is a shallow layer of inflow at most radii below the outflow with two local maxima, one with a speed of $1.6 \text{ m}\cdot\text{s}^{-1}$ at a radius just inside that of maximum outflow and another slightly weaker one near a radius of 200 km.

By 60 hr, the lower inflow layer between 9 and 11 km has strengthened and now extends to the outer radius shown (300 km), with a maximum speed of $4.8 \text{ m}\cdot\text{s}^{-1}$, while a shallower, but weaker layer of inflow has developed just above the outflow layer between 15 and 17 km. In addition, there are weaker layers of inflow, one between about 8 and 10 km and the other between 17 and 19 km,

but these would appear to be transient features as they are not prominent at 74 hr. At 60 hr, the mean eyewall updraught, delineated by the $0.25 \text{ m}\cdot\text{s}^{-1}$ contour of mean vertical velocity has strengthened since 42 hr. By 74 hr, strengthening of the upper-level outflow and the inflow layers sandwiching it is evident (Figure 2f) as well as a broadening of the mean eyewall updraught complex.

The green dashed contours in Figures 2b, d, f enclose areas of mean subsidence with sinking rates larger than $0.02 \text{ m}\cdot\text{s}^{-1}$. At 42 hr, these areas are generally small and patchy, but at later times they become more coherent. At 60 and 74 hr there is a shallow area of enhanced subsidence just above and beyond where the eyewall terminates, suggesting that the eyewall updraught overshoots its equilibrium level and adjusts back to this level as it flows outwards. There are large areas of enhanced subsidence also in the low to mid troposphere, outside the eyewall updraught complex, inside a radius between about 150–200 km, and on the inner edge of this complex.

At 60 hr, there is a region of enhanced subsidence beyond 200 km radius which overlaps with part of the outflow layer and all of the inflow layer below it. There is another region of subsidence between 50 and 75 km radius where this inflow layer terminates adjacent to the eyewall updraught complex.

At 74 hr, a large area of enhanced subsidence has developed below the outflow layer between about 80 km and 210 km. This region overlaps with the inflow layer just below the outflow. At this time there is an inflow maximum also within the eyewall complex itself, which is connected to a narrow region of subsidence separating two areas of eyewall updraught. Animations of the fields indicate that this deep finger of subsidence and the inflow maximum to which it is connected are transient features, which by 76 hr have disappeared (not shown). We show later that the flow in the upper troposphere, including the eyewall region, has a marked azimuthal wavenumber-one asymmetry at these times.

Having documented the existence and evolving structure of upper-level inflow layers, the natural question that emerges is what their impact is on the storm structure? We address this question in the next subsection.

3.3 | Effects of the inflow layers on storm evolution

Animations of vertical cross-sections at 15 min intervals during the intensification period shows a progressive inward movement of the \bar{M} -surfaces with a prominent inward-pointing nose in the inflow layer just above the outflow layer. At lower altitudes, the animations show a pronounced folding of individual \bar{M} -surfaces to produce

transient ‘z-like’ patterns with an outward-pointing nose at large radius in the outflow layer and an inward pointing nose that is sometimes in the outflow layer and at other times in the inflow layer below it. These upper-level features are exemplified in Figures 2b, d, f and are to be expected as the \bar{M} surfaces are initially closer to the vertical than to the horizontal and \bar{M} is approximately materially conserved in the upper troposphere, at least beyond the eyewall updraught. These \bar{M} -surfaces are strongly distorted by the vertical gradient of mean radial flow.

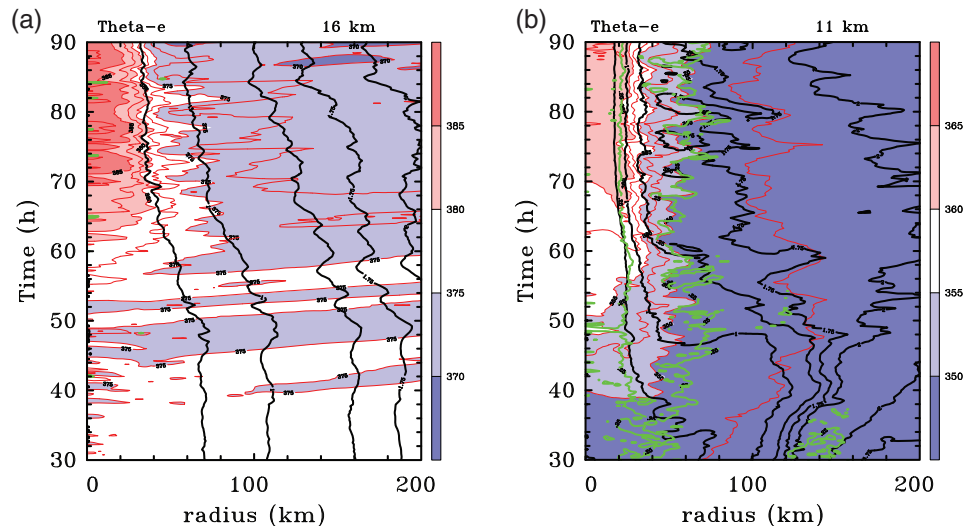
Figure 3 shows radius–time cross-sections of \bar{M} -contours at altitudes of 16 and 11 km, together with similar contours of azimuthally averaged equivalent potential temperature, $\bar{\theta}_e$. Also shown at these levels is the contour of vertical velocity with a magnitude of $0.25 \text{ m}\cdot\text{s}^{-1}$ to indicate the approximate location of the eyewall updraught complex at this level. Beyond this updraught complex, the quantities \bar{M} and $\bar{\theta}_e$ should be approximately materially conserved by the mean radial flow.

At 16 km altitude, which is within the inflow layer above the outflow layer and slightly above the eyewall updraught complex, an inward migration of the \bar{M} -surfaces is clearly evident, at least within a radius of 180 km. This inward migration implies a spin-up of the mean tangential wind at this level. There is an inward migration of the \bar{M} -surfaces at 11 km altitude also, but in the inner region, within the eyewall updraught, the inward migration can be attributed in part to the upward advection of tangential momentum.³ There is an event in Figure 3b where an \bar{M} -surface appears to form at a finite radius and subsequently move inwards (e.g., at 79 hr at a radius of about 100 km). This occurrence is associated with the passage of the inward- and downward-moving tip of a folding \bar{M} -surface through the level in question. After about 60 hr, as the inflow below the outflow layer strengthens, the migration at radii larger than 100 km occurs in oscillatory pulses with a period of a few hours. Whatever the circumstance, the inward migrating \bar{M} -surface implies a spin-up of the mean tangential wind within this inflow layer.

Like the \bar{M} -surfaces, the $\bar{\theta}_e$ -surfaces are approximately materially conserved in three dimensions, but these surfaces are nearly horizontal at the initial time and they are subsequently distorted in a different way. At 16 km altitude (Figure 3a), $\bar{\theta}_e$ shows little change with the contour interval chosen until just after 60 hr, except for a

³Here and within the terminus of the upper-level eyewall complex we observe also instances of folding \bar{M} surfaces and the formation of closed \bar{M} -contours (islands) associated with the upward advection of \bar{M} -surfaces by convective updraughts and the differential stretching of these surfaces by the inflow and outflow (not shown). The intricate dynamics of these events warrants further study and will be discussed elsewhere.

FIGURE 3 Radius–time cross sections at (a) 16 km, and (b) 11 km, based on 15 min output of azimuthally averaged pseudo-equivalent potential temperature, $\bar{\theta}_e$ (red contours with 2.5 K interval and shading), absolute angular momentum, \bar{M} (black contours with $0.5 \times 10^6 \text{ m}^2 \cdot \text{s}^{-1}$ interval plus extra contour at $1.75 \times 10^6 \text{ m}^2 \cdot \text{s}^{-1}$) and vertical velocity \bar{w} (green contour at 0.25 $\text{m} \cdot \text{s}^{-1}$, indicating the approximate location of the eyewall updraught)



slight reduction at most radii (between 45 and 50 hr) and small positive pulses inside a radius of 50 km. These pulses reflect the effect of convective updraughts that occasionally reach this level during the earlier period of evolution. Beyond 60 hr, the eyewall convective complex begins to persist at this altitude as reflected in the increase of $\bar{\theta}_e$ values most prominently within about 60 km radius. As there is radial inflow at this level (e.g., Figures 2b, d, f), this region of elevated $\bar{\theta}_e$ values remains radially confined.

The situation is similar at 11 km altitude (Figure 3b), where the increase in $\bar{\theta}_e$ values occurs a little earlier at about 40 hr but, as at 16 km, the increase remains radially confined by the inflow. The presence of a weak negative radial gradient of $\bar{\theta}_e$ at this level is indicated by the red contour ($\bar{\theta}_e = 347.5 \text{ K}$) between 90 km and 140 km radius and beyond about 45 hr. Note that the fluctuations in the radial location of this contour are closely correlated with those of \bar{M} indicating that beyond the eyewall updraught complex, both $\bar{\theta}_e$ and \bar{M} are approximately conserved in radial displacements at 11 km.

Animations of vertical cross-sections of $\bar{\theta}_e$ and \bar{M} show that the surfaces of these quantities have significantly different structure during much of the intensification phase, but with some tendency for the surfaces to become more parallel in the eyewall updraught region during the later stages of intensification (after about 72 hr) and into the mature stage (not shown). A particularly striking feature of these surfaces during this later stage is the way in which advection by the radial inflow beneath the outflow layer leads to a more vertically erect eyewall and effectively reinforces the eyewall $\bar{\theta}_e$ front in the upper troposphere.

The vertically coherent eyewall front is evident in Figure 4, which shows vertical cross-sections of $\bar{\theta}_e$ at 60 and 74 hr with the \bar{M} -surfaces and selected contours of radial and vertical velocity superimposed. The distribution of $\bar{\theta}_e$ shows the classical structure. The principal features

are: the mid-tropospheric minimum beyond a radius of about 100 km, increasing in prominence with radius; the tendency for the isopleths of $\bar{\theta}_e$ to become close to vertical in the eyewall updraught complex; and the tendency for these isopleths to slope outwards and become close to horizontal in the upper-tropospheric outflow layer. There is an approximate congruence between the $\bar{\theta}_e$ and \bar{M} surfaces in the eyewall updraught complex above about 5 km and in the upper troposphere where the air ascending in the eyewall flows outwards.

Throughout much of the troposphere, $\bar{\theta}_e$ has a negative radial gradient. This is, in part, a reflection of the structure in the boundary layer. Although this description broadly captures the basic reason for the interior $\bar{\theta}_e$ structure, the inner-core region underneath the eyewall complex (radius $< 25 \text{ km}$) exhibits a somewhat more intricate structure. Here there is a local region of enhanced radial gradient in which the eye appears to act as a source of high $\bar{\theta}_e$ air (Figure 4). This air rises into the eyewall updraught, effectively feeding the updraught with enhanced $\bar{\theta}_e$ (not shown). The finger of enhanced $\bar{\theta}_e$ is clearly evident at 60 hr and becomes more pronounced at 74 hr. This low-level $\bar{\theta}_e$ structure has been observed and analyzed elsewhere by Zhang *et al.* (2001) with a similar interpretation.

The role of nonlinear boundary-layer dynamics in creating this corner structure in $\bar{\theta}_e$ is certainly an interesting and important topic, but lies outside the scope of the current study.

Returning to the upper-level structure of $\bar{\theta}_e$, and recalling the approximate material conservation of this quantity, a prominent feature to note is the development between 60 and 74 hr of subsidence of lower-stratospheric air into the upper part of the eye with the strongest subsidence occurring in a finger along the inside edge of the eyewall (Figure 4b). Another prominent feature is the broadening

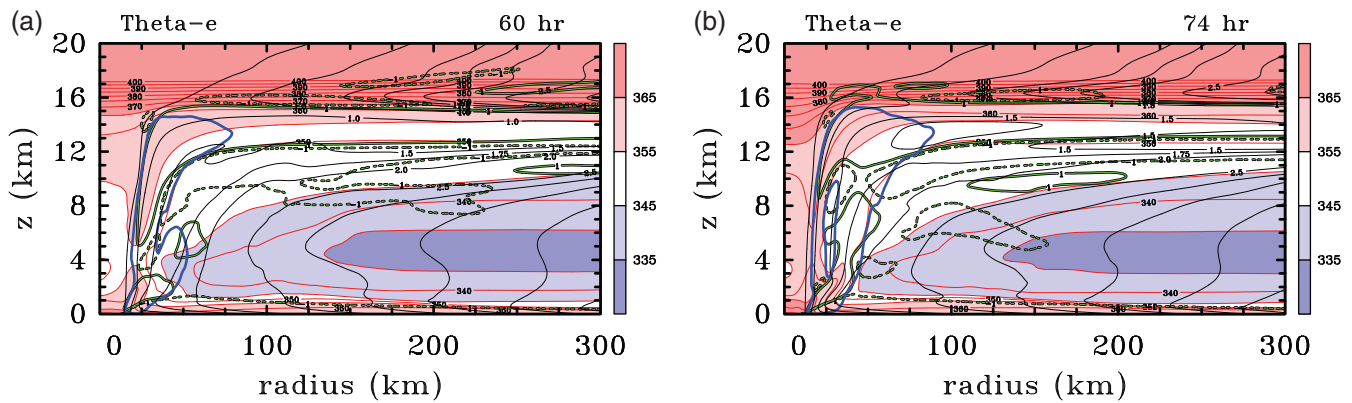


FIGURE 4 Radius–height cross sections at (a) 60 hr and (b) 74 hr of pseudo-equivalent potential temperature, $\bar{\theta}_e$ (red contours with shading and interval 5 K), and absolute angular momentum, \bar{M} (black contours with interval $0.5 \times 10^6 \text{ m}^2 \cdot \text{s}^{-1}$ and an extra contour at $1.75 \times 10^6 \text{ m}^2 \cdot \text{s}^{-1}$). Superimposed on each panel are two (green) contours of the radial velocity component \bar{u} at $\pm 1 \text{ m} \cdot \text{s}^{-1}$ (solid and dashed), and one (thick blue) contour of the vertical velocity component, \bar{w} ($0.25 \text{ m} \cdot \text{s}^{-1}$ to indicate the approximate location of the eyewall updraught). All fields are azimuthally averaged and time-averaged for one hour using 1 min output.

of the eyewall updraught complex during this period, which is related, at least in part, to the (transient) splitting of the updraught at 74 hr.

The effect of the upper-layer inflow on the $\bar{\theta}_e$ field is harder to discern from a comparison of Figures 4a and b than it is in the animations. This is due to the broadening of the eyewall updraught complex during this period, a broadening that is evident also in the $\bar{\theta}_e$ pattern in Figure 3b, and the fact that $\bar{\theta}_e$ values in the updraught have increased. However, as suggested by the inward movement of the $\bar{\theta}_e$ surfaces beyond the eyewall updraught complex in Figure 3b, the convergent inflow must play a role in tightening the radial gradient of $\bar{\theta}_e$ in the upper troposphere on the outside of the eyewall.

3.4 | Cause of the inflow layers

As a starting point to understand the origin of the layers of inflow sandwiching the upper-level outflow, we carry out an analysis of the azimuthally averaged radial momentum equation in the cylindrical coordinate system (r, λ, z) , which can be written in the following form:

$$\begin{aligned} \frac{\partial \bar{u}}{\partial t} + \underbrace{\bar{u} \frac{\partial \bar{u}}{\partial r}}_{U_{mr}} + \underbrace{\left(u' \frac{\partial u'}{\partial r} + \frac{v'}{r} \frac{\partial u'}{\partial \lambda} \right)}_{U_{eh}} = & \\ - \underbrace{\bar{w} \frac{\partial \bar{u}}{\partial z}}_{U_{mv}} - \underbrace{\bar{w}' \frac{\partial u'}{\partial z}}_{U_{ev}} + \underbrace{\frac{\bar{v}^2}{r} + f \bar{v} - \frac{1}{\bar{\rho}} \frac{\partial \bar{p}}{\partial r}}_{U_{magf}} + \underbrace{\frac{\bar{v}'^2}{r} - \frac{1}{\bar{\rho}} \frac{\partial \bar{p}'}{\partial r}}_{U_{eagf}} & \\ + \underbrace{\frac{1}{\bar{r} \bar{\rho}} \frac{\partial \bar{r} \bar{\rho}}{\partial r} \bar{\tau}_{rr}}_{U_{dh}} - \underbrace{\frac{\bar{\tau}_{\lambda \lambda}}{r}}_{U_{dv}} + \underbrace{\frac{1}{\bar{\rho}} \frac{\partial \bar{\rho}}{\partial z} \bar{\tau}_{rz}}_{U_{dv}}, & \quad (1) \end{aligned}$$

where here, for any quantity α , $\alpha' = \alpha - \bar{\alpha}$ denotes a departure from the azimuthal mean, or eddy component, t is the time, u, v, w are the radial, tangential and vertical components of velocity, ρ is the density, p is the pressure, f is the Coriolis parameter, ζ is the vertical component of relative vorticity, and the stress tensors τ_{rr} , $\tau_{\lambda \lambda}$ and τ_{rz} (generalized to account for anisotropic eddy momentum diffusivities) for the subgrid-scale motions can be calculated from:

$$\overline{\tau_{rr}} = 2K_{m,h} \left(\frac{\partial u}{\partial r} \right), \quad (2)$$

$$\overline{\tau_{\lambda \lambda}} = 2K_{m,h} \left(\frac{1}{r} \frac{\partial v}{\partial \lambda} + \frac{u}{r} \right), \quad (3)$$

$$\overline{\tau_{rz}} = K_{m,v} \left(\frac{\partial w}{\partial r} + \frac{\partial u}{\partial z} \right) \quad (4)$$

(e.g. Landau and Lifshitz 1966, p. 51). Here $K_{m,h}$ and $K_{m,v}$ are the horizontal and vertical diffusivities of horizontal momentum⁴.

To facilitate interpretation, we have chosen this pseudo-Lagrangian form in which the left-hand side of Equation (1) represents the material acceleration in the radial direction following the horizontal wind. The reason for this choice is to provide a layer-wise perspective of the generation of inflow and outflow layers. The individual terms on this side represent: the local tendency of the mean radial velocity, the mean radial advection of radial momentum per unit mass, U_{mr} , and the mean horizontal

⁴The expression for $\overline{\tau_{rz}}$ corrects the expression given in Persing *et al.* (2013) (their equation (20)) and Montgomery and Smith (2017) (their equation (15)). The difference is found to be negligible.

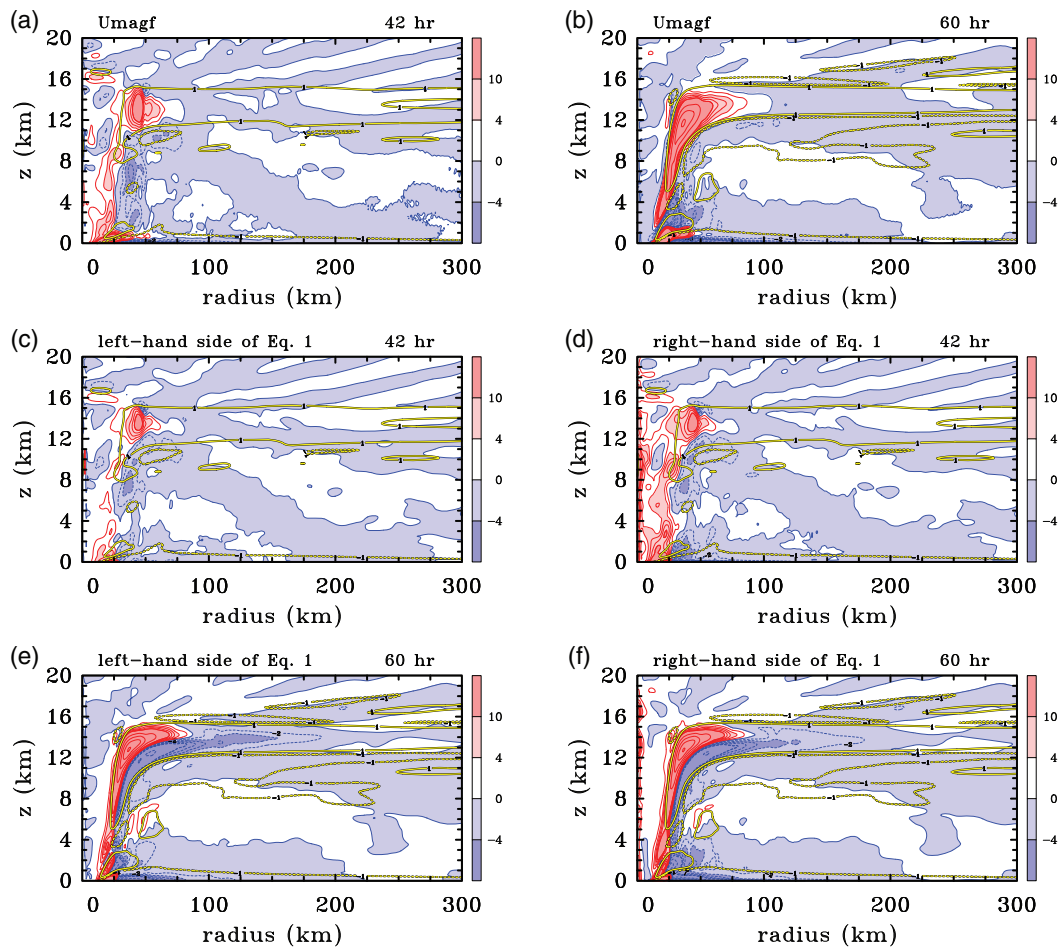


FIGURE 5 Radius–height cross sections of the main terms in the azimuthally averaged radial momentum equation (Equation (1)) with two contours ($\pm 1 \text{ m}\cdot\text{s}^{-1}$, solid and dashed yellow thick contour with black border) of the azimuthally averaged radial velocity component, \bar{u} , superimposed. (a, b) mean agradiant force per unit mass, U_{magf} ; (c, e) left-hand side of Equation (1); (d, f) right-hand side of Equation (1) at (c, d) 42 hr and (e, f) 60 hr. All fields are azimuthally averaged and time-averaged for 1 hr using 1 min output. The contour interval for terms in the momentum equation is $2 \text{ m}\cdot\text{s}^{-1}\cdot\text{hr}^{-1}$ for values from 0 to $\pm 10 \text{ m}\cdot\text{s}^{-1}\cdot\text{hr}^{-1}$, and $10 \text{ m}\cdot\text{s}^{-1}\cdot\text{hr}^{-1}$ for values higher in magnitude (red solid contours for positive values, blue dashed contours for negative values).

advection of eddy radial momentum per unit mass, U_{eh} . The terms on the right-hand side of Equation (1) are in order: U_{mv} is minus the mean vertical advection of mean radial momentum per unit mass and U_{ev} is minus the eddy vertical advection of eddy radial momentum per unit mass; U_{magf} and U_{eagf} are the mean and eddy agradiant force per unit mass, respectively; U_{dh} is the mean horizontal diffusive tendency of radial momentum while U_{dv} is the vertical diffusive tendency.

Figure 5 shows radius–height cross-sections of some main terms in the azimuthally averaged and 1 hr time-averaged radial momentum equation centred at 42 and 60 hr. The fields are overlain with the azimuthally and time-averaged radial velocity. Figures 5a, b show the mean agradiant force field, U_{magf} , which characterizes the degree of gradient wind imbalance, at 42 and 60 hr, respectively. Prominent features of this field at both times include:

- A shallow layer of strong subgradient force ($U_{magf} < 0$) beyond a radius of 25 km. This layer corresponds with the frictional boundary layer in which the negative force imbalance drives a strong, surface-based inflow (Figures 2b and 2d);
- A deeper region of supergradient force ($U_{magf} > 0$) immediately inside this radius and extending above the shallow subgradient force region. This force serves to decelerate the boundary-layer inflow and accelerate outflow just above the inflow layer as the air ascends into the eyewall;
- A region of subgradient force through the lower troposphere extending beyond a radius of 200 km. This force accelerates air inwards towards the eyewall and accounts for the spin-up of the tangential winds above the boundary layer outside the developing eyewall (radii $> 50 \text{ km}$).

- At 60 hr (Figure 5b), a tower of supergradient force within the outward-sloping eyewall updraught from about 2 km to 15 km in height. In this region, air with high tangential momentum generated in the boundary-layer inflow is lofted into the eyewall updraught. This lofting is sufficiently strong that the sum of the centrifugal and Coriolis forces exceeds the inward radial pressure gradient force per unit mass as air parcels ascend. In turn, the outward force drives these air parcels outwards as they ascend. At 42 hr (Figure 5a), this structure has not yet become established.

From about 13 km to 15 km, the region of strong positive $Umagf$ extends to a radius of about 75 km at 42 hr and 100 km at 60 hr. This force is the main outward force accelerating the upper-level outflow. As air parcels move outwards in this region, while approximately conserving their absolute angular momentum, their tangential velocity diminishes. Eventually, the inward-directed pressure gradient force present at this level finally gains the upper hand and the sign of $Umagf$ reverses. This sign change of $Umagf$ is to be expected since mass continuity requires the outflowing air parcels to decelerate as the flow spreads out. Invoking Newton's second law of motion, the only way that air parcels can decelerate radially is if they experience a negative radial force. Recall that in fluid flows, the pressure force is determined as part of the solution and is constrained globally by the boundary conditions on the flow as well as the need to satisfy mass continuity and Newton's second law of motion.

An equivalent way to think about the outflow layer is to consider it as an expanding jet of air emanating from a mass and radial momentum source where the eyewall convection terminates (Ooyama, 1987). The outward expansion is resisted by an induced radially inward pressure gradient force (recall that the centrifugal force is always positive and the Coriolis force in the radial direction is positive as long as the tangential flow remains cyclonic). Because the induced pressure field extends beyond just the outflow layer itself, one can expect a flow response vertically beyond the outflow layer as well. In confirmation of this idea, Figure 5b shows that $Umagf$ is mostly inward beyond a radius of 100 km (beyond 75 km in Figure 5a), not only in the outflow layer itself, but over a significant depth above and below it, especially below. Where this inward force persists, it will act to accelerate air parcels inwards.

The foregoing interpretation appears to be different from that proposed by Komaromi and Doyle (2017) to explain the inflow above the outflow layer, which they believe "to be associated with a 'reverse' secondary circulation pattern, associated with dry-adiabatic descent above the eye in the lower stratosphere". It is unclear whether

the "belief" rests on balance ideas, whether it invokes an unbalanced argument in which descent in the eye "sucks air inwards" above the tropopause, or whether it is pure speculation.

From a balance dynamics perspective, the proffered explanation seems unlikely because the subsiding air on the inside of the eyewall updraught would be explained as a result of the diabatic heating in the eyewall itself (Schubert *et al.*, 2007). The balance response to this heating would be limited by the local Rossby scale, which for a fully developed tropical cyclone vortex in the eyewall is on the order of 60 km (Shapiro and Montgomery, 1993). Therefore, the idea of the upper-level inflow, which extends beyond 300 km at the later times shown, being a balanced consequence of the diabatic heating in the upper eyewall cloud seems problematic and implausible to us⁵.

Consider a more general perspective not limited to balance. Since the pressure field is connected globally by the requirement that the mass continuity equation is globally satisfied and since the vortex is a tightly coupled system through the pressure field, it is clear that if air is being funnelled towards the eye just above the tropopause it must either ascend or descend in the central region. The high static stability in the stratosphere would overwhelmingly favour descent into the eye and, from an unapproximated, unbalanced perspective, according to Newton's second law, the pressure field would have to adjust to drive this descent. In this view, whether one argues that the eye "sucks air inwards" or that the flow in the upper inflow layer is driven by the inward gradient force may be a matter of semantics.

In developing the foregoing interpretation for the emergence and persistence of the upper-level inflow layers that straddle the main outflow layer, we note that the solution for the upper-troposphere region is highly variable in both time and azimuth. This behaviour is a result of inertia-gravity waves that are generated by transient deep convection. Consequently, the persistence of this underlying forcing structure tends to be obscured in individual snapshots of the flow and becomes evident only after time averaging on the scale of an hour or two. The effects of inertia-gravity wave fluctuations in the upper-level outflow and inflow layers as well as the outflow just above where the inflowing boundary-layer inflow terminates are evident as fluctuations in the extrema in radial wind in Figure 1b.

The essence of the radial momentum budget is encapsulated in Figures 5c–f. These show the sum of the time-averaged and azimuthally averaged tendencies on

⁵Indeed, an explicit balance calculation presented in Section 5 confirms this argument. In particular, the balance flow is radially outward in the lower stratosphere outside of the eyewall cloud.

each side of Equation (1) at 42 and 60 hr. Figure 5c, e show the time-averaged pseudo-Lagrangian radial acceleration, while Figure 5d, f show the corresponding time-averaged net radial force leading to this acceleration. At both times, there is generally good agreement between the pseudo-radial acceleration and the net forcing terms, especially in the upper troposphere, which is the centre point of this paper. These comparisons provide confidence in the integrity of the calculations. In the lower troposphere, there are a few local discrepancies in detail between the acceleration and forcing terms. These are presumably associated with interpolation errors and the like (Montgomery *et al.*, 2020, section 4.2.1).

3.5 | Asymmetric structure of outflow and inflow layers

Figure 6 shows horizontal cross-sections of the radial velocity component u (red/blue) along with horizontal wind vectors and vertical velocity w (yellow) at different levels at selected times. The vortex centre at each level, indicated by the hurricane symbol, is calculated in the same way as described in the Appendix. The left panels show cross-sections at a height of approximately 11 km (actually 11.16 km) that is generally within the upper-level inflow layer beneath the outflow layer, while the right columns show the fields at a height of approximately 14 km (actually 14.29 km), which is within the outflow layer itself.

Early on in the intensification stage, at 42 hr, there is outflow in all sectors beyond a radius of about 40 km at 14 km height (Figure 6b), with mostly inflow inside this radius. The inflow is seen to occur on the inside edges of deep convective cores, which lie predominantly outside a radius of 30–40 km. The situation at 11 km is rather different (Figure 6a), with mostly inflow in the northern half of the domain and mostly outflow in the southern half (here we refer to the y -direction as north, even though in the problem as formulated on an f -plane, there is no preferred direction). Clearly, the inflow layer at this altitude and time is quite asymmetric.

At 60 hr, towards the end of the intensification stage, the outflow at 14 km has strengthened and is to a first approximation symmetric with outflow at all azimuths about the centre (Figure 6d). The inflow at 11 km has strengthened also, but is seen to retain a significant degree of asymmetry, being most extensive in the northeastern sector and least extensive in the southwestern sector. Broadly, the inflow lies outside an annulus of outflow coinciding with the eyewall updraught at this altitude. Noteworthy is the fact that the region of inflow with a magnitude exceeding $5 \text{ m}\cdot\text{s}^{-1}$ contains elongated bands

of both enhanced ascent and descent that are presumably some form of wave motions (inertia-buoyancy waves and/or vortex Rossby waves).

At 74 hr, during the quasi-steady mature stage, the outflow at 14 km exceeds $15 \text{ m}\cdot\text{s}^{-1}$ beyond a radius of 50–100 km that depends on azimuth (Figure 6f). At this level there is a weak inflow within 20 km in a region south of the centre. However, at 11 km (Figure 6e), the pattern of inflow and outflow remains asymmetric with an inward counterclockwise spiralling band of inflow extending from about 120 km eastsoutheast of the vortex centre to about 50 km east of the centre, where it terminates. At radii inside this band is an inward counterclockwise spiralling band of outflow that extends from approximately southwest of the vortex centre to the north of the centre.

The pattern of azimuthal-mean radial and vertical motion at 74 hr in Figure 2f shows a deep, radially confined downdraught that apparently splits the eyewall updraught. The upper portion of this downdraught corresponds to an upper-level inflow maximum at a radius of about 30 km and an altitude between 9 and 10 km. We investigate the degree of symmetry of this feature in Figure 7, which shows similar horizontal cross-sections to those in Figures 6e and f, but at altitudes of 6.1 km and 9.9 km. Like the higher altitudes at this time, the pattern of inflow and outflow at both levels exhibits a marked asymmetry.

At 9.9 km altitude (Figure 7b), the pattern has a prominent azimuthal wavenumber-one component, with spiral regions of inflow and outflow, much like the pattern at 11 km in Figure 6e and the orientation of the spiral pattern is much the same. The main difference is the localized region of stronger inflow in the east to southeast sector at 9.9 km, at radii between about 15 and 35 km, which would account for the local maximum of inflow near 10 km altitude seen in Figure 2f. On the broad scale, it is apparent that most of the strongly inflowing air is descending. At 6.1 km altitude (Figure 7a), the localized region of inflow is smaller in area and rotated slightly counterclockwise. At both altitudes, only part of the region of localized inflow coincides with a region of subsidence.

Further investigation of the inner-core asymmetric structure is tangential to the main aims of this paper and we will not pursue such an investigation here. Nevertheless, because the explanation given in Section 3.4 is presented from an axisymmetric viewpoint, it is appropriate to consider its applicability in the light of the low azimuthal wavenumber asymmetric structure of the inflow layers shown in Figures 6 and 7. Since the principal asymmetry of the upper tropospheric flow is azimuthal wavenumber one, and since the argument presented for the existence of the inflow jets invokes a vertical extension of the pressure field above and below the outflow layer, one might argue that the forcing of the inflow layers would apply equally to

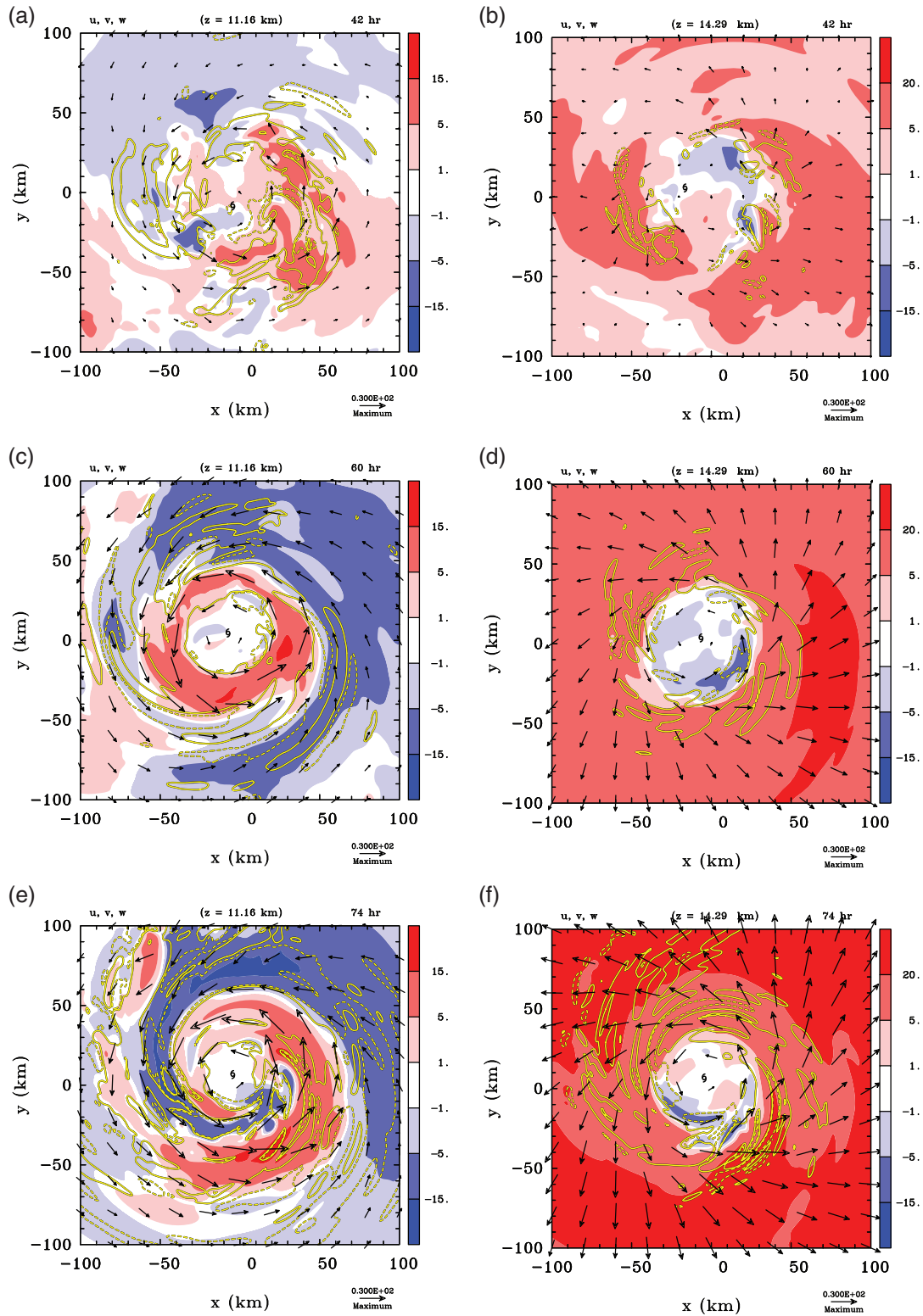


FIGURE 6 Instantaneous, horizontal cross sections of the radial velocity component, u (m s^{-1} , shaded contours), horizontal wind vectors, and vertical velocity, w (two yellow contours at ± 0.5 m s^{-1} , solid and dashed), at (a, b) 42 hr, (c, d) 60 hr, and (e, f) 74 hr for heights (a, c, e) 11 km and (b, d, f) 14 km. The maximum reference wind vector is 30 m s^{-1} shown on the lower right corner. The vortex centre, indicated by the hurricane symbol, is defined as the location of minimum wind speed at each particular level

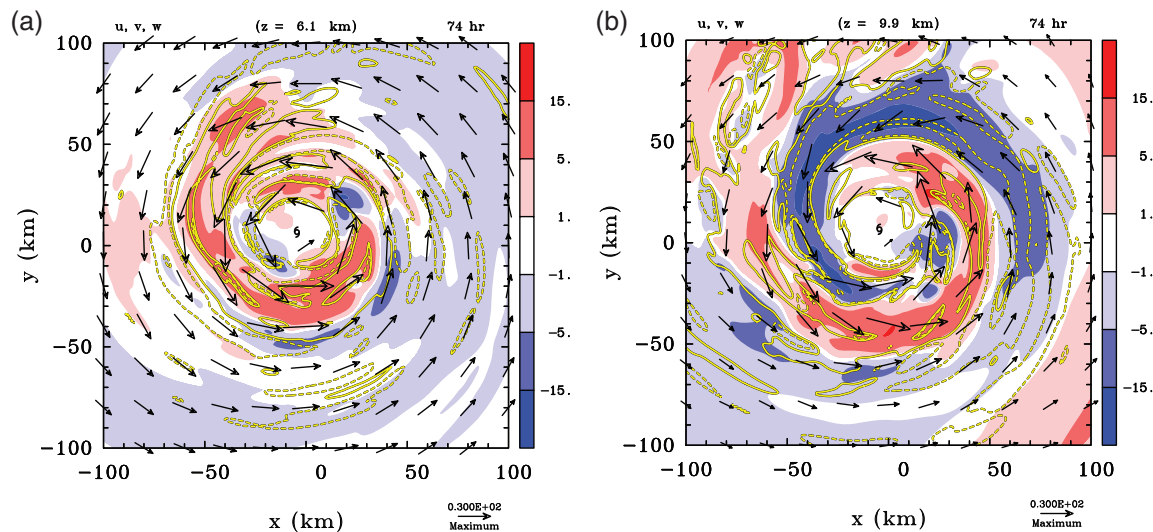


FIGURE 7 Instantaneous, horizontal cross sections of the radial velocity component, u ($\text{m}\cdot\text{s}^{-1}$, colour shading), horizontal wind vectors, and vertical velocity, w (two yellow contours at $\pm 0.5 \text{ m}\cdot\text{s}^{-1}$, solid and dashed), at heights of (a) 6.1 km and (b) 9.9 km, both at 74 hr. The maximum reference wind vector is $30 \text{ m}\cdot\text{s}^{-1}$ shown on lower right corner. The vortex centre, indicated by the hurricane symbol, is defined as the location of minimum wind speed at each particular level

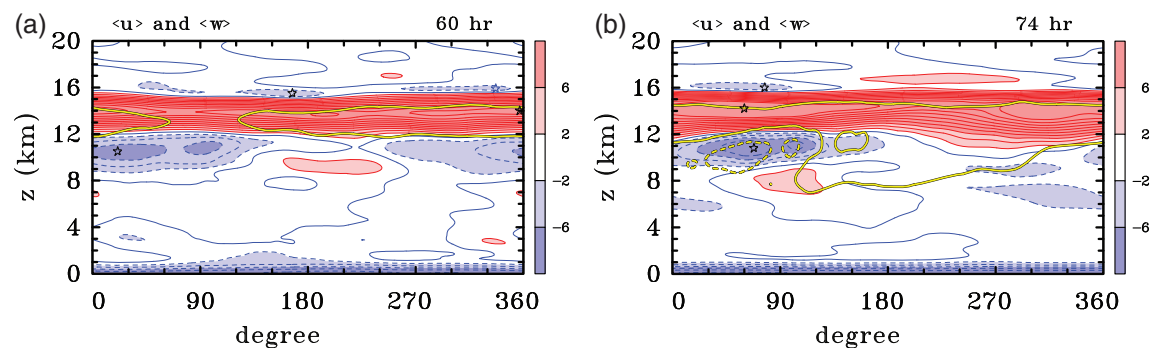


FIGURE 8 Azimuth–height cross sections of the 1 hr time-averaged (based on 1 min output) radial velocity component, $\langle u \rangle$ (shaded contours with interval $2 \text{ m}\cdot\text{s}^{-1}$, red solid for positive, blue dashed for negative), and vertical velocity, $\langle w \rangle$ (two yellow thick contours at $\pm 0.25 \text{ m}\cdot\text{s}^{-1}$, solid and dashed), both averaged over an annulus from $r = 50$ to 100 km , at (a) 60 hr and (b) 74 hr. Shading values on colour bar. Black star symbols denote locations of maximum inflow and outflow in the upper troposphere; the blue star in (a) is a local maximum inflow. The “east” direction corresponds with 0° and azimuth is measured counterclockwise

a sector of the upper-tropospheric flow region. To examine this possibility, we show in Figure 8 azimuth–height cross-sections of the mean radial motion in an annular region between radii 50 and 100 km at 60 and 74 hr. At both these times, the mean upper-tropospheric outflow is more axisymmetric than the mean inflow just below it.

At 60 hr, the inflow layer below the outflow layer is concentrated mostly in the sector going counterclockwise from approximately south (270° in Figure 8a) to the northwest (135°) with a maximum value 25° to the north of east and a minimum in the southwest (225°). At 74 hr (Figure 8b), the outflow layer has thickened and developed two local maxima while the inflow has become more azimuthally confined and the maximum inflow has

rotated counterclockwise to about 15°E of north. At both times, the outflow is seen to be still ascending, while at 74 hr, much of the lower inflow layer overlaps with a region of subsidence. These features may be seen from the two contours of vertical velocity in Figure 8b with a magnitude of $0.25 \text{ m}\cdot\text{s}^{-1}$, the contour with the negative value being dashed.

If the argument is correct that the forcing of the upper inflow layers applies equally to a sector, then, subject to the caveat at the end of this paragraph, the sector with maximum inflow should correspond approximately with the sector with maximum outflow. At both times in Figure 8, the azimuth of maximum inflow below the outflow is close to that of maximum outflow, the separation distance being

about 20° at 60 hr and less than 10° at 74 hr. At 74 hr, the same is true of the maximum inflow above the outflow, but at 60 hr, the situation is less clear. At this time there are three sectors of enhanced inflow above the outflow and the strongest inflow maximum (near 180°) lies far from that of the outflow maximum. Even so, there is a local inflow maximum at about 340° , within 20° of the outflow maximum.

Further support for the role of the agradient force in producing the inflow layers is obtained by examination of the azimuthal variation of the agradient force field as a function of height (not shown). Such plots indicate that the regions of maximum upper-level inflow coincide on average with regions of maximum inward agradient forcing at these levels.

Overall, the foregoing findings point to the robustness of the argument that the inward agradient force is producing the upper-level inflow layers. Even though the occurrence of inflow above and below the outflow layer does not occur at all values of azimuth, the interpretation for the presence of inflow is based on the existence of an inward agradient force that either decelerates outflow or accelerates inflow. Thus, one does not necessarily expect a one-to-one correspondence everywhere between inward acceleration and inflow. Another complication is the possibility that, during vortex evolution, there may be occasional bouts of moderately deep convection that detrain in particular sectors at a lower level than the outflow layer itself.

Clearly, the asymmetric structure of the upper-tropospheric outflow and inflow layers is complex, in part, because of the significant internal variability forced by deep convection as well as the inertia-buoyancy waves, vortex Rossby waves and possibly other instabilities excited by this convection (e.g., Anthes 1972; Chen *et al.*, 2003; Flatau and Stevens 1993; Reasor and Montgomery 2015) and it would be simplistic to expect that an argument based on symmetric reasoning would be correct in all details. However, we believe the interpretations given above are defensible.

4 | OBSERVATIONS

Traditionally, it has been difficult to obtain detailed measurements of the upper-troposphere flow in tropical cyclones as this region tends to be above the ceiling of conventional jet aircraft. The situation changed with the recent deployment of the NASA Global Hawk to survey storms. The Global Hawk is an autonomous aircraft drone that can overfly storms and release dropsondes into them from the lower stratosphere. One such study of cyclone structure based on such soundings is

that by Komaromi and Doyle (2017). These authors show, *inter alia*, radius–height cross-sections of radial wind for two composite datasets obtained from dropsondes into six non-developing or developing storms (their figures 8a,c, respectively). Both these composites show layers of inflow above and below the upper-tropospheric outflow layer, but a little surprisingly, the inflow layer beneath the outflow layer is stronger in the case of the non-developing storms.

In their figure 10, Komaromi and Doyle (2017) show individual radius–height cross-sections of radial wind for four storms in their dataset and in their figure 11 they show vertical cross-sections of radial flow averaged from 100 to 500 km radius. Again, these data show layers of inflow above and below the upper-tropospheric outflow layer.

Another observational study is that by Smith *et al.* (2019), which presented vertical cross-sections of wind and thermodynamic fields obtained in Atlantic *Hurricane Edouard* (2014), one of the storms investigated also by Komaromi and Doyle. Figure 1c of Smith *et al.* (2019) shows a radius-height cross-section of mean radial flow constructed from the dropsonde data obtained over an 18 hr period on 16–17 September. This cross-section shows that, above a height of 10 km, there are significant layers of inflow straddling the upper-tropospheric outflow layer.

Duran and Molinari (2018) described an observational analysis of the upper troposphere and lower stratosphere of rapidly intensifying *Hurricane Patricia* (2015) in which they showed two vertical cross-sections of the storm-relative radial and tangential velocities in the lower stratosphere based on dropsonde data (their figure 10). They stated that the radial cross sections corroborate the existence of a lower-stratospheric inflow layer connected to descent in the eye, but the data shown are hard to relate to the inflow layer structure found in our simulations.

Overall, the observational findings are not surprising in view of the propensity of numerical models to show the development of upper-tropospheric inflow layers, even though in reality, such inflow layers may be significantly influenced by the effects of environmental vertical wind shear that is normally present in real cases.

5 | ON A BALANCE THEORY FOR INFLOW JETS

Long ago, Willoughby (1979) presented a scale analysis of the equations of motion for a tropical cyclone and showed that, with the exception of the frictional boundary layer and possibly parts of the upper-level outflow, the flow in a tropical cyclone is in approximate gradient wind balance and hydrostatic balance. With these balance assumptions one can then develop a prognostic theory for axisymmetric

tropical cyclone evolution (e.g., Ooyama 1969; Sundqvist 1970a, 1970b; Schubert and Alworth 1970b; Emanuel 1989; Möller and Smith 1994; Smith *et al.* 2018a; Smith and Wang 2018).

In a subsequent paper, drawing on a previous result of Eliassen (1951), Shapiro and Willoughby (1982) noted that the response of the secondary circulation to a positive point source of tangential momentum is radially outwards through the source, following a nearly horizontal isentropic surface, and radially inwards above and below the source (their figure 1). A cyclonic source of azimuthal-mean tangential momentum had been thought of as a mechanism for enhancing the upper-level outflow in a tropical cyclone (Challa and Pfeffer 1980 and references; Molinari and Vollaro 1990 and references; Montgomery and Farrell 1993), which would act as a catalyst for inducing the intensification process. The origin of such a source was attributed to “eddy forcing” resulting from flow asymmetries and/or potential vorticity anomalies in the upper-level outflow region. It follows that the radially inward flow above and below such a tangential momentum source might provide an alternative explanation for the existence of upper-tropospheric inflow layers as studied here. Such a possibility needs exploring.

The foregoing ideas are illustrated in Figure 9, which shows in (b) the balanced response to the hypothetical lens of tangential momentum forcing, $-\dot{V}(r, z)$, in (a). The calculation assumes a tangential wind structure with a maximum of $50 \text{ m}\cdot\text{s}^{-1}$ at a radius of 25 km at the surface. The tangential wind decreases sinusoidally with height to an altitude of 20 km and is zero above 20 km. This vortex is everywhere symmetrically stable. The wind structure is indicated by the solid contours in Figure 9a. The corresponding balanced distribution of pressure and temperature are obtained using the unapproximated method of Smith (2006), assuming a latitude of 20°N and the Dunion moist tropical sounding (Dunion, 2011) at some large radius. The equation solved for the streamfunction of the secondary circulation is the most general form detailed by Smith *et al.* (2005) and Smith *et al.* (2018a).

As in the case of a point source of tangential momentum, the secondary circulation forced by $-\dot{V}(r, z)$ in Figure 9a comprises a layer of outflow through the source and two layers of inflow sandwiching this outflow. The difference in vertical extent and strength between the upper and lower inflow layers is presumably related, in part, to the differences in inertial stability, $I^2 = \xi\zeta_a$, and static stability, $N^2 = (g/\theta)\partial\theta/\partial z$, within or in the vicinity of these layers. Here ξ is twice the azimuthally averaged absolute angular velocity, ζ_a is the azimuthally averaged absolute vorticity, θ is the balanced potential temperature and g is the acceleration due to gravity.

Figure 9c,d show the separate diagnosed contributions from generalized (including eddy terms implicitly) diabatic heating and tangential momentum forcing from the numerical simulation in conjunction with the azimuthally averaged tangential wind field from the simulation at 60 hr. The principal feature of the diabatic heating is a tower of heating inside a radius of about 50 km with two radial tongues of heating centred at heights of about 13 and 15 km. There are narrow regions of cooling along the inner eyewall, a shallow finger of cooling just near the tropopause, and some isolated patches of cooling outside the eyewall. The main regions of momentum forcing are in the boundary layer and in the developing eyewall. These panels show also regions of negative I^2 , in which the flow is inertially unstable, and regions of negative discriminant of the Sawyer–Eliassen equation (e.g., Bui *et al.*, 2009, equation (15)).

Figures 9e,f show the balanced secondary circulation associated with the respective heating and momentum forcing in Figures 9c and 9d, while Figure 9g shows the total balanced secondary circulation solution at 60 hr and Figure 9h shows that in the simulation at the same time. Notably, the secondary circulation associated with the diabatic heating dominates that associated with the momentum forcing (compare (e) and (f)) and, in particular, accounts for much of the upper-level inflow above and below the outflow layer (compare (e) and (g)) in the balance solution.

Comparison of the balanced secondary circulation with the azimuthally averaged circulation in the simulation indicates that the mean height of the outflow is too low (12 km compared with 14 km) and the outflow is split at larger radii in the balance solution. There are strong discrepancies also in the strength and radial extent of the inflow layer. For example, the inflow below the outflow layer is approximately twice as strong in the balance solution and the inflow layer above the outflow layer is barely evident. The boundary-layer inflow in the balance solution is significantly weaker than in the simulation (maximum inflow $8.3 \text{ m}\cdot\text{s}^{-1}$ compared with $24.5 \text{ m}\cdot\text{s}^{-1}$), but is much deeper in the inner region, supporting findings of Montgomery and Persing (2020). However, in order to obtain a convergent solution for the balanced secondary circulation, we needed to coarsen the interpolated simulation data to 2 km in the radial direction and 500 m in the vertical direction. The computational domain consists of a cylindrical region 200 km in radius and 20 km in height. Amongst other things, this coarsening shrinks the region in which the discriminant of the Sawyer–Eliassen equation is negative (not shown) and suggests a fundamental limitation of balance dynamics for highly resolved tropical-cyclone-like flows. This point is underscored by our cursory application of the balance inversion at other

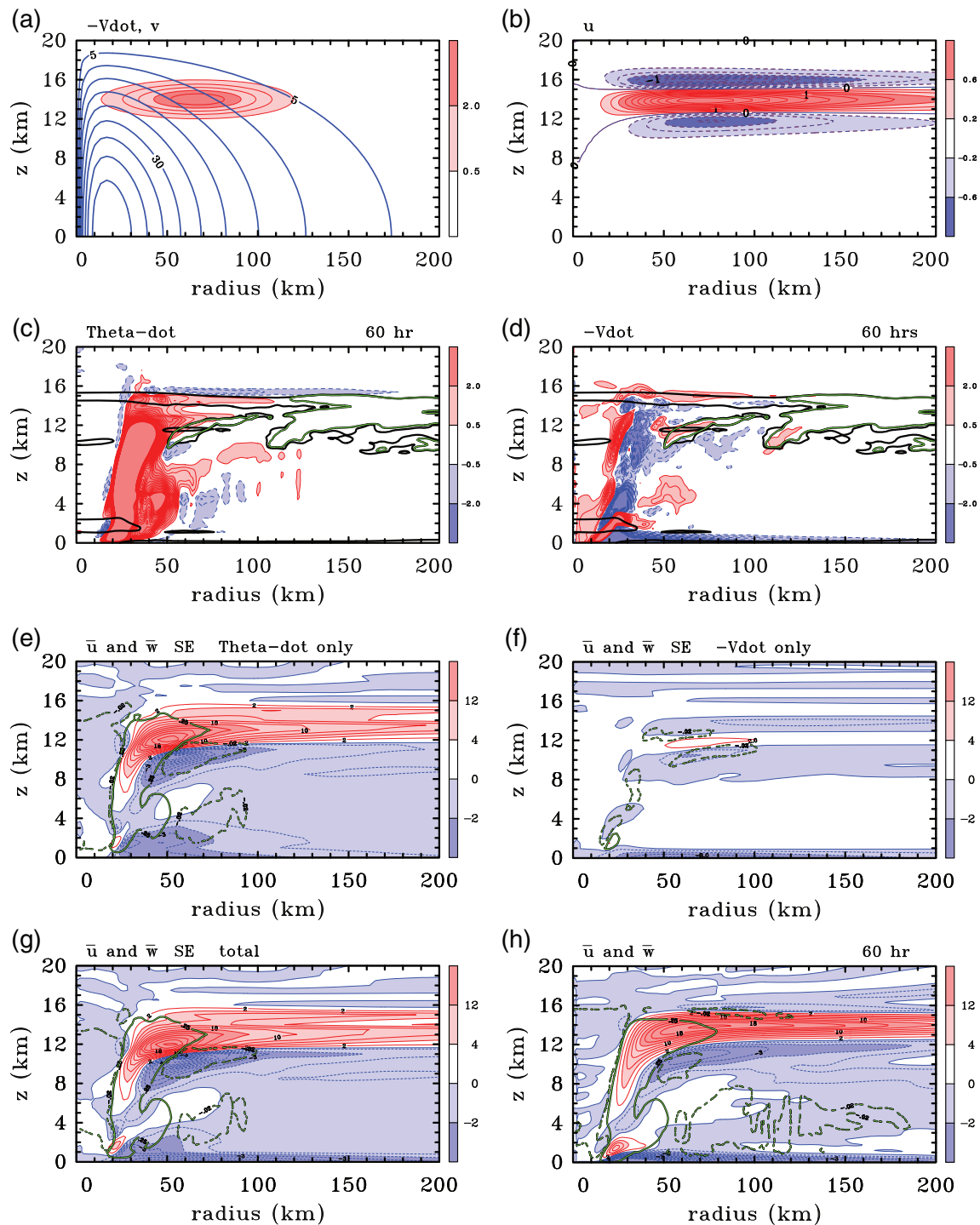


FIGURE 9 Axisymmetric balanced solution of an idealized TC-like vortex to a prescribed tangential momentum forcing in the upper troposphere. (a) tangential velocity (blue thick contours with interval $5 \text{ m}\cdot\text{s}^{-1}$) and upper-level tangential momentum source, $-\dot{V}(r, z)$ (red contours with interval $0.5 \text{ m}\cdot\text{s}^{-1}\cdot\text{hr}^{-1}$) and (b) radial velocity component of the axisymmetric balanced secondary circulation induced by this forcing (contour interval $0.25 \text{ m}\cdot\text{s}^{-1}$). For comparison, (c, d) show the (c) generalized diabatic heating (contour interval $0.5 \text{ K}\cdot\text{hr}^{-1}$) and (d) generalized tangential momentum forcing (contour interval $0.5 \text{ m}\cdot\text{s}^{-1}\cdot\text{hr}^{-1}$) from the numerical simulation at 60 hr. (e, f) show the corresponding balanced secondary circulation associated with the separate (c) heat forcing and (d) momentum forcing. (g) shows the total balanced secondary circulation solution at 60 hr and (h) shows that in the simulation at the same time. The fields in (c, d, h) are azimuthally averaged and time-averaged for 1 hr using 1 min output. Contour intervals for \bar{u} are $2 \text{ m}\cdot\text{s}^{-1}$ when $\bar{u} > 0$, $1 \text{ m}\cdot\text{s}^{-1}$ when $\bar{u} < 0$. In (c, d), the green contour is that of zero inertial stability, while the black contour is that of the zero discriminant. In (e–h), \bar{w} is shown by two green thick contours at $0.25 \text{ m}\cdot\text{s}^{-1}$ and $-0.02 \text{ m}\cdot\text{s}^{-1}$ (solid and dashed).

times. Our experience suggests that a coarsened solution is typically possible at 60 hr and before. However, at later times the regions of negative discriminant become too extensive in the outflow layer and even regularization is inadequate to achieve a convergent solution⁶.

In summary, the balance secondary circulation broadly reproduces the main features of the simulated circulation and indicates that the balanced inflow below the upper-level outflow layer arises from the spatial gradients of the diabatic heating rate in conjunction with the regularization procedure. In terms of the balance model, the inflow is just that required to keep the main vortex in thermal wind balance in the presence of heat forcing. In other words, this inflow is the response needed to keep the vortex in balance.

That this overturning circulation broadly captures the main feature of the simulated flow is, in fact, a consequence of imposing the vertical mass flux associated with the diabatic heating rate. For this flow regime, the vertical velocity is largely obtained by balancing the adiabatic cooling with the diabatic heating and hence the vertical velocity is essentially proportional to the diabatic heating rate. Given the rapidly rotating environment of the hurricane and the strongly nonlinear forcing associated with the frictional boundary, there is no reason to expect the detailed features of the simulation to match those of the balance calculation.

The inability of the balance calculation to capture the secondary circulation in the simulation quantitatively is not surprising and consistent with the fact that, as shown in the next section, there are large regions in the upper troposphere where the gradient wind balance approximation is nowhere near satisfied. The same can be said about the low-level inflow layer in the inner-core region where the maximum tangential winds are being generated.

Furthermore, there are large regions in the upper troposphere where the discriminant of the Sawyer–Eliassen equation for the secondary circulation is negative (the regions enclosed by black curves in Figures 9c and d). In that case, to obtain a strictly balanced solution, one can only invert the Sawyer–Eliassen equation by modifying (or regularizing) the coefficients in such a way that the equation is rendered elliptic. However, the recent study of such regularization procedures by Wang and Smith (2019) has shown that the secondary circulation within and near these upper-level unstable regions is particularly sensitive to the way in which the regularization is carried out, especially where the forcing overlaps

with these regions. This sensitivity, which will be explored further in a separate paper, casts doubt on the reliability of any inference based on balance ideas. It is worth noting that the main region where the two fields in Figures 9g and h show a significant departure is precisely where the discriminant of the Sawyer–Eliassen equation is negative.

In the light of these considerations, it would appear that a more fundamental framework for understanding the secondary circulation and the implied tangential wind tendency associated with it is needed. We would argue that a return to Newton's second law of motion is the recommended path for improved understanding. In this framework, balance is not an imposed constraint on the flow dynamics.

6 | AXISYMMETRIC BALANCE THEORY AND ITS LIMITATIONS

Since the magnitude of $Umagf$ is a measure of the degree of force imbalance in the radial direction, the fields shown in Figure 5 provide a context to assess the accuracy of the balance theory of tropical cyclones, in general, and thereby its applicability to explaining the upper-tropospheric inflow jets in particular.

In his review paper on the tropical cyclone inner core, Willoughby (1988, p. 186) wrote “Although the wind may be supergradient where the boundary-layer inflow decelerates under the eyewall, the role of the imbalance in the secondary circulation has been exaggerated.” More recently, Heng *et al.* (2017) claimed that “balanced dynamics can well capture the secondary circulation in the full-physics model simulation *even in the inner-core region in the boundary layer* [italics added]”. These claims were called into question long ago by the analysis of a three-dimensional numerical simulation of *Hurricane Andrew* (1992) by Zhang *et al.* (2001), which showed significant imbalances in the boundary layer, just above it, and through much of the eyewall⁷.

The simulation by Zhang *et al.* (2001) had a relatively coarse 6 km horizontal grid spacing by modern standards, compared with the 1 km used in the present simulations, and it was performed for a particular storm. In comparison, the idealized calculation presented here is carried out in a quiescent environment. For these reasons it is of interest to examine the extent to which Zhang *et al.*'s findings are generic. As a contribution to the debate on the accuracy of the balance approximation, we show in Figure 10 radius–height cross sections of $Umagf$ normalized by the

⁶The results shown in Figure 9 have been verified by an independent multi-grid solver of the Sawyer–Eliassen equation. The results of these comparisons will be reported in a separate publication.

⁷These claims have been refuted more recently also by Montgomery and Persing (2020).

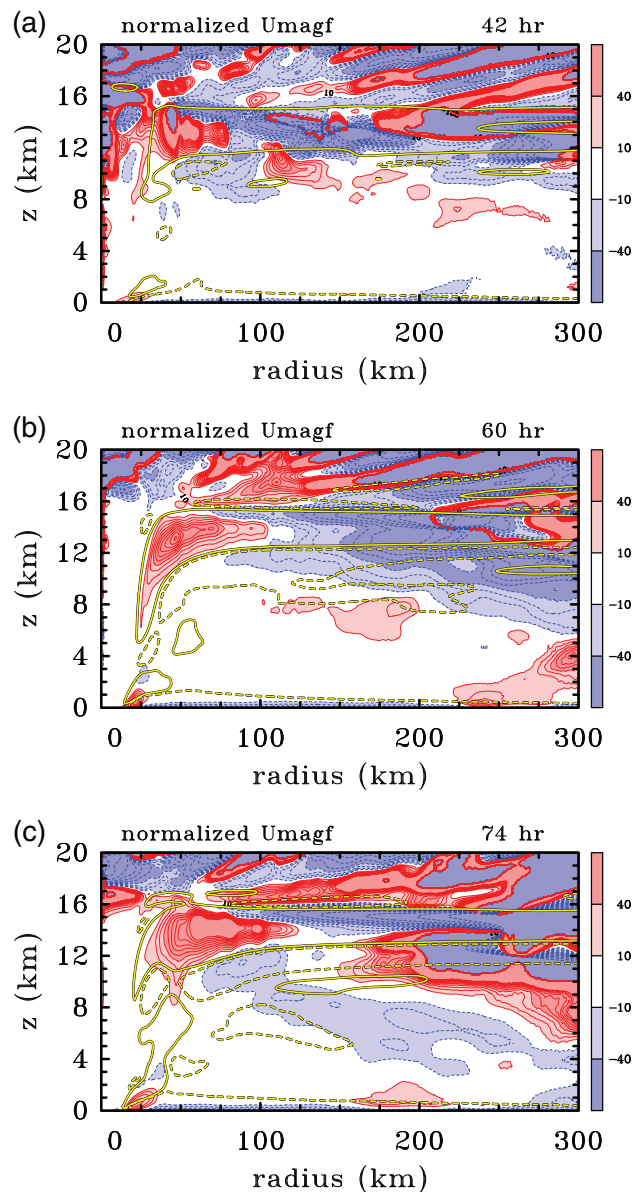


FIGURE 10 Radius–height cross sections at (a) 42 hr, (b) 60 hr, and (c) 74 hr of U_{magf} normalized by the radial pressure gradient force (shaded contours, solid red for positive, blue dashed for negative values, with interval 10% from -100% to 100%), with two (yellow) thick contours superimposed of the azimuthal mean radial velocity component, \bar{u} ($\pm 1 \text{ m s}^{-1}$, solid and dashed). All fields are azimuthally averaged and time-averaged for 1 hr using 1 min output.

local radial pressure gradient and expressed as a percentage: $U_{magf} / [(1/\bar{\rho})(\partial\bar{p}/\partial r)]$.

At all times shown (42, 60 and 74 hr), much of the upper troposphere shows significant force imbalance (magnitude of normalized U_{magf} approaching 100% supergradient at the top of the eyewall and exceeding 50% subgradient in much of outer region of outflow). At 60 and 74 hr, in the outer part of the frictional boundary layer (beyond about 25 km radius), the force imbalance is as

much as 30% subgradient. At smaller radii and low levels near the base of the eyewall, the normalized imbalance exceeds 40% supergradient. In contrast, much of the low to mid troposphere is balanced to within 10%, especially at 42 and 60 hr. These findings are broadly in line with those of Zhang *et al.* (figure 6d and related discussion), but they do highlight also a significant degree of relative imbalance characterized by significant values of normalized U_{magf} in the upper-tropospheric outflow layer⁸. One difference is that Zhang *et al.* did not find inflow layers, perhaps because the vertical resolution of their simulation was insufficient, or because of the presence of significant vertical wind shear.

7 | CONCLUSIONS

Three-dimensional numerical simulations of tropical cyclone intensification with moderately high vertical resolution have been used to analyze the development of a layer of strong inflow beneath the upper-tropospheric outflow layer as well as, in some cases, a shallower layer of weaker inflow above the outflow layer. The calculations pertain to the prototype problem for tropical cyclone intensification, which considers the evolution of a vortex on an f -plane in a quiescent environment starting from an initially symmetric, moist, cloud-free vortex over a warm ocean.

The analyses presented endorse a previous idea of Ooyama (1987) to view the outflow layer as an expanding jet of air emanating from a radial mass and momentum source where the eyewall convection terminates. They suggest also a new way to think about the inflow layers above and below the outflow layer. From an azimuthally averaged perspective, we showed that the outflow itself is driven near its source primarily by a positive agradient force in which the centrifugal and Coriolis force in the radial direction is partly opposed by the radially inward pressure gradient force. As air parcels move outwards, approximately conserving their absolute angular momentum, the tangential velocity diminishes as does the sum of the centrifugal and Coriolis forces. Well beyond the source, the inward-directed radial pressure gradient force begins to dominate and leads to a deceleration of the outflow. The inward pressure gradient force extends vertically above and below the outflow layer itself, and leads to a flow response on either side of the outflow layer, where it accelerates air parcels inwards.

⁸These results are consistent also with the degree of relative axisymmetric imbalance shown in Schecter (2018, figure 1b).

An alternative explanation for the inflow layers in terms of axisymmetric balance dynamics was shown to be problematic. Moreover, it was shown that there is a significant degree of imbalance in the upper troposphere.

Observational evidence for the existence of the inflow layers sandwiching the outflow layer was reviewed and prior explanations for the inflow layers were appraised.

The inflow layers adjacent to the upper-level outflow were shown to have a role in modifying the vortex structure in the upper troposphere. The inflow layer above the outflow layer leads to a spin-up of the tangential winds there, thereby extending the cyclonic circulation of the hurricane vertically. In addition, the inflow acts to resist the radial spread of air with high equivalent potential temperature at this level. The inflow layer below the outflow layer leads also to a spin-up of the cyclonic tangential winds in the inflow layer and would appear to contribute to an increase of the magnitude of the radial gradient of equivalent potential temperature at the outer edge of the eyewall.


The inflow layers adjacent to the upper-level outflow were shown to be more asymmetric than the outflow layer itself, having a low azimuthal wavenumber flow asymmetry. Nevertheless, the region of maximum inflow above and below the outflow layer tends to align with that of maximum outflow, which, in a first approximation, supports the foregoing interpretation of the inflow layers based on axisymmetric reasoning.

In summary, this work outlines a new framework for examining the outflow and inflow layer dynamics in tropical cyclone vortices. Further work on the asymmetric aspects of these layers, as well as an understanding of their modification in more complex environments, would be of meteorological and fluid dynamical interest.

ACKNOWLEDGEMENT

MTM acknowledges the support of NSF grants AGS-1313948, IAA-1656075, ONR grant N0001420WX01473, and the U.S. Naval Postgraduate School. The views expressed herein are those of the authors and do not represent sponsoring agencies or institutions. SW acknowledges a PhD stipend from the China Scholarship Council.

ORCID

Shanghong Wang  <https://orcid.org/0000-0002-0773-3448>

Roger K. Smith  <https://orcid.org/0000-0002-3668-1608>

Michael T. Montgomery  <https://orcid.org/0000-0001-5383-4648>

REFERENCES

- Anthes, R.A. (1972) Development of asymmetries in a three-dimensional numerical model of the tropical cyclone. *Monthly Weather Review*, 100, 461–476.
- Braun, S.A., Newman, P.A. and Heymsfield, G.M. (2016) NASA's Hurricane and Severe Storm Sentinel (HS3) investigation. *Bulletin of the American Meteorological Society*, 97, 2085–2102.
- Bryan, G.H. (2012) Effects of surface-exchange coefficients and turbulence length scales on the intensity and structure of numerically simulated hurricanes. *Monthly Weather Review*, 140, 1125–1143.
- Bryan, G.H. and Morrison, H. (2012) Sensitivity of a simulated squall line to horizontal resolution and parameterization of microphysics. *Monthly Weather Review*, 140, 202–225.
- Bryan, G.H. and Rotunno, R. (2009) Evaluation of an analytical model for the maximum intensity of tropical cyclones. *Journal of the Atmospheric Sciences*, 66, 3042–3060.
- Bu, Y.P., Fovell, R.G. and Corbosiero, K.L. (2014) Influence of cloud-radiative forcing on tropical cyclone structure. *Journal of the Atmospheric Sciences*, 71, 1644–1622.
- Bui, H.H., Smith, R.K., Montgomery, M.T. and Peng, J. (2009) Balanced and unbalanced aspects of tropical-cyclone intensification. *Quarterly Journal of the Royal Meteorological Society*, 135, 1715–1731.
- Challa, M. and Pfeffer, R. (1980) Effects of eddy fluxes of angular momentum on model hurricane development. *Journal of the Atmospheric Sciences*, 37, 1603–1618.
- Chen, H. and Zhang, D.-L. (2013) On the rapid intensification of hurricane *Wilma* (2005). Part II: convective bursts and the upper-level warm core. *Journal of the Atmospheric Sciences*, 70, 146–162.
- Chen, X., Xue, M. and Fang, J. (2018) Rapid intensification of typhoon *Mujigae* (2015) under different sea surface temperatures: structural changes leading to rapid intensification. *Journal of the Atmospheric Sciences*, 75, 4313–4335.
- Chen, Y., Brunet, G. and Yau, M.K. (2003) Spiral bands in a simulated hurricane. Part II: wave activity diagnosis. *Journal of the Atmospheric Sciences*, 60, 1239–1256.
- Doyle, J.D., Moskaitis, J.R., Feldmeier, J.W., Ferek, R.J., Beaubien, M., Bell, M.M., Cecil, D.L., Creasey, R.L., Duran, P., Elsberry, R.L., Komaromi, W.A., Molinari, J., Ryglicki, D.R., Stern, D.P., Velden, C.S., Wang, X., Allen, T., Barrett, B.S., Black, P.G., Dunion, J.P., Emanuel, K.A., Harr, P.A., Harrison, L., Hendricks, E.A., Hendon, D., Jeffries, W.Q., Majumdar, S.J., Moore, J.A., Pu, Z., Rogers, R.F., Sanabia, E.R., Tripoli, G.J. and Zhang, D.-L. (2017) A view of tropical cyclones from above: the tropical cyclone intensity experiment. *Bulletin of the American Meteorological Society*, 98, 2113–2134.
- Dunion, J.P. (2011) Rewriting the climatology of the tropical North Atlantic and Caribbean Sea atmosphere. *Journal of Climate*, 24, 893–908.
- Duran, P. and Molinari, J. (2018) Dramatic inner-core tropopause variability during the rapid intensification of hurricane *Patricia* (2015). *Monthly Weather Review*, 146, 119–134.
- Duran, P. and Molinari, J. (2019) Tropopause evolution in a rapidly intensifying tropical cyclone: a static stability budget analysis in an idealized axisymmetric framework. *Journal of the Atmospheric Sciences*, 76, 209–229.

- Eliassen, A. (1951) Slow thermally or frictionally controlled meridional circulation in a circular vortex. *Astrophysica Norvegica*, 5, 19–60.
- Emanuel, K.A. (1989) The finite-amplitude nature of tropical cyclogenesis. *Journal of the Atmospheric Sciences*, 46, 3431–3456.
- Emanuel, K.A. (2012) Self-stratification of tropical cyclone outflow. Part II: implications for storm intensification. *Journal of the Atmospheric Sciences*, 69, 988–996.
- Flatau, M. and Stevens, D.E. (1993) The role of outflow-layer instabilities in tropical cyclone motion. *Journal of the Atmospheric Sciences*, 50, 1721–1733.
- Fovell, R.G., Bu, Y.P., Corbosiero, K.L., Tung, W.-W., Cao, Y., Kuo, H.-C., Hsu, L.-H. and Su, H. (2016) Influence of cloud microphysics and radiation on tropical cyclone structure and motion. *Meteorological Monographs*, 56, 11.1–11.27.
- Hausman, S.A., Ooyama, K.V. and Schubert, W.H. (2006) Potential vorticity structure of simulated hurricanes. *Journal of the Atmospheric Sciences*, 63, 87–108.
- Heng, J., Wang, Y. and Zhou, W. (2017) Revisiting the balanced and unbalanced aspects of tropical cyclone intensification. *Journal of the Atmospheric Sciences*, 74, 2575–2591.
- Kieu, C., Tallapragada, V., Zhang, D.-L. and Moon, Z. (2016) On the development of double warm-core structures in intense tropical cyclones. *Journal of the Atmospheric Sciences*, 73, 4487–4506.
- Komaromi, W.A. and Doyle, J.D. (2017) Tropical cyclone outflow and warm-core structure as revealed by HS3 dropsonde data. *Monthly Weather Review*, 145, 1339–1359.
- Landau, L.D. and Lifshitz, E.M. (1966) *Fluid Mechanics* (Third Revised English Edition). Pergamon Press, Oxford, UK.
- Molinari, J. and Vollaro (1990) External influences on hurricane intensity. Part II: vertical structure and the response of the hurricane vortex. *Journal of the Atmospheric Sciences*, 47, 1902–1918.
- Möller, J.D. and Smith, R.K. (1994) The development of potential vorticity in a hurricane-like vortex. *Quarterly Journal of the Royal Meteorological Society*, 120, 1255–1265.
- Montgomery, M.T. and Farrell, B.F. (1993) Tropical cyclone formation. *Journal of the Atmospheric Sciences*, 50, 285–310.
- Montgomery, M.T. and Persing, J. (2020) Does balance dynamics well capture the secondary circulation and spin-up of a simulated tropical cyclone?. *Journal of the Atmospheric Sciences*, 77.
- Montgomery, M.T. and Smith, R.K. (2014) Paradigms for tropical cyclone intensification. *Australian Meteorological and Oceanographic Society Journal*, 64, 37–66.
- Montgomery, M.T. and Smith, R.K. (2017) Recent developments in the fluid dynamics of tropical cyclones. *Annual Review of Fluid Mechanics*, 49, 541–574.
- Montgomery, M.T. and Smith, R.K. (2019) Toward understanding the dynamics of spin up in Emanuel's tropical cyclone model. *Journal of the Atmospheric Sciences*, 76, 3089–3093.
- Montgomery, M.T., Persing, J. and Smith, R.K. (2019) On the hypothesized outflow control of tropical cyclone intensification. *Quarterly Journal of the Royal Meteorological Society*, 145, 1309–1322.
- Montgomery, M.T., Kilroy, G., Smith, R.K. and Črnivec, N. (2020) Contribution of mean and eddy momentum processes to tropical cyclone intensification. *Quarterly Journal of the Royal Meteorological Society*, 146. <https://doi.org/10.1002/qj.3837>
- Nguyen, V.S., Smith, R.K. and Montgomery, M.T. (2008) Tropical-cyclone intensification and predictability in three dimensions. *Quarterly Journal of the Royal Meteorological Society*, 134, 563–582.
- Ohno, T. and Satoh, M. (2015) On the warm core of a tropical cyclone formed near the tropopause. *Journal of the Atmospheric Sciences*, 72, 551–571.
- Ooyama, K.V. (1969) Numerical simulation of the life cycle of tropical cyclones. *Journal of the Atmospheric Sciences*, 26, 3–40.
- Ooyama, K.V. (1987) *Numerical experiments of steady and transient jets with simple model of the hurricane outflow layer* Vol. 17, pp. 318–320). Miami, FL: American Meteorological Society. Preprint.
- Persing, J., Montgomery, M.T., McWilliams, J. and Smith, R.K. (2013) Asymmetric and axisymmetric dynamics of tropical cyclones. *Atmospheric Chemistry and Physics*, 13, 12 299–12 341.
- Rappin, E.D., Morgan, M.C. and Tripoli, G.J. (2011) The impact of outflow environment on tropical cyclone intensification and structure. *Journal of the Atmospheric Sciences*, 68, 177–194.
- Reasor, P.D. and Montgomery, M.T. (2015) Evaluation of a heuristic model for tropical cyclone resilience. *Journal of the Atmospheric Sciences*, 72, 1765–1782.
- Rotunno, R. and Emanuel, K.A. (1987) An air–sea interaction theory for tropical cyclones. Part II: evolutionary study using a nonhydrostatic axisymmetric numerical model. *Journal of the Atmospheric Sciences*, 44, 542–561.
- Schecter, D.A. (2018) On the instabilities of tropical cyclones generated by cloud-resolving models. *Tellus A*, 70. <https://doi.org/10.1080/16000870.2018.1525245>
- Schubert, W.H. and Alworth, B.T. (1982) Evolution of potential vorticity in tropical cyclones. *Quarterly Journal of the Royal Meteorological Society*, 39, 1687–1697.
- Schubert, W.H., Slocum, C.J., Vigh, J.L., McNoldy, B.D. and Kossin, J.P. (2007) On the distribution of subsidence in the hurricane eye. *Quarterly Journal of the Royal Meteorological Society*, 133, 1–20.
- Shapiro, L.J. and Montgomery, M.T. (1993) A three-dimensional balance theory for rapidly rotating vortices. *Journal of the Atmospheric Sciences*, 50, 3322–3335.
- Shapiro, L.J. and Willoughby, H. (1982) The response of balanced hurricanes to local sources of heat and momentum. *Journal of the Atmospheric Sciences*, 39, 378–394.
- Smith, R.K. (2006) Accurate determination of a balanced axisymmetric vortex. *Tellus A*, 58, 98–103.
- Smith, R.K. and Montgomery, M.T. (2015) Towards clarity on understanding tropical cyclone intensification. *Journal of the Atmospheric Sciences*, 72, 3020–3031.
- Smith, R.K. and Wang, S. (2018) Axisymmetric balance dynamics of tropical cyclone intensification: diabatic heating versus surface friction. *Quarterly Journal of the Royal Meteorological Society*, 144, 2350–2357.
- Smith, R.K., Montgomery, M.T. and Zhu, H. (2005) Buoyancy in tropical cyclone and other rapidly rotating atmospheric vortices. *Dynamics of Atmospheres and Oceans*, 40, 189–208.
- Smith, R.K., Montgomery, M.T. and Persing, J. (2014) On steady-state tropical cyclones. *Quarterly Journal of the Royal Meteorological Society*, 140, 2638–2649.
- Smith, R.K., Montgomery, M.T. and Bui, H. (2018a) Axisymmetric balance dynamics of tropical cyclone intensification and its breakdown revisited. *Journal of the Atmospheric Sciences*, 75, 3169–3189.
- Smith, R.K., Montgomery, M.T. and Kilroy, G. (2018b) The generation of kinetic energy in tropical cyclones revisited. *Quarterly Journal of the Royal Meteorological Society*, 144, 2481–2490.

- Smith, R.K., Montgomery, M.T. and Braun, S.A. (2019) Azimuthally averaged structure of hurricane *Edouard* (2014) just after peak intensity. *Quarterly Journal of the Royal Meteorological Society*, 145, 211–216.
- Stern, D.P., Kepert, J.D., Bryan, G. and Doyle, J.D. (2020) Understanding atypical mid-level wind speed maxima in hurricane eyewalls. *Journal of the Atmospheric Sciences*, 77. early view online.
- Sundqvist, H. (1970a) Numerical simulation of the development of tropical cyclones with a ten-level model. Part I. *Tellus*, 4, 359–390.
- Sundqvist, H. (1970b) Numerical simulation of the development of tropical cyclones with a ten-level model. Part II. *Tellus*, 5, 505–510.
- Tao, D., Emanuel, K.A., Zhang, F., Rotunno, R., Bell, M.M. and Nystrom, R.G. (2019) Evaluation of the assumptions in the steady-state tropical cyclone self-stratified outflow using three-dimensional convection-allowing simulations. *Journal of the Atmospheric Sciences*, 76, 2995–3009.
- Wang, S. and Smith, R.K. (2019) Consequences of regularizing the Sawyer–Eliassen equation in balance models for tropical cyclone behaviour. *Quarterly Journal of the Royal Meteorological Society*, 145, 3766–3779.
- Willoughby, H.E. (1979) Forced secondary circulations in hurricanes. *Journal of Geophysical Research*, 84, 3173–3183.
- Willoughby, H.E. (1988) The dynamics of the tropical cyclone core. *Australian Meteorological Magazine*, 36, 183–191.
- Zhang, D.-L. and Chen, H. (2012) Importance of the upper-level warm core in the rapid intensification of a tropical cyclone. *Geophysical Research Letters*, 39(L02). <https://doi.org/10.1029/2011GL050578>
- Zhang, D.-L., Liu, Y. and Yau, M.K. (2001) A multi-scale numerical study of hurricane *Andrew* (1992). Part IV: unbalanced flows. *Monthly Weather Review*, 61, 92–107.

How to cite this article: Wang S, Smith RK, Montgomery MT. Upper-tropospheric inflow layers in tropical cyclones. *QJR Meteorol Soc.* 2020;146:3466–3487. <https://doi.org/10.1002/qj.3856>

APPENDICES

APPENDIX A. APPRAISAL OF KIEU *ET AL.*'S EXPLANATION FOR UPPER-TROPOSPHERIC INFLOW LAYERS

In their study examining the development of double warm-core structures in intense tropical cyclones, Kieu *et al.* (2016) observed the formation of an upper-level inflow layer (UIL), located in the lower stratosphere, above the upper-level outflow layer. These authors offered three tentative explanations for the UIL (see below) based on a Lagrangian integration of an equation for the quantity $S = \partial u / \partial z$, the azimuthal vorticity (in the hydrostatic approximation). In their analysis, the development of an

inflow layer above the outflow layer is associated with the development of negative azimuthal vorticity. Assuming that parcels start with zero azimuthal vorticity at the base of the eyewall cloud (an assumption that does not appear to be justified), they find that evolution of the azimuthal vorticity depends on a time integral along the parcel trajectory of a forcing function that is in part proportional to the departure from thermal wind balance A , where $A = -(R/H)\partial T/\partial r + \Omega\partial v/\partial z$, where R denotes the ideal gas constant for dry air, H denotes the scale height, T denotes the temperature, $\Omega = f + 2v/r$ denotes twice the absolute rotation rate and $\partial v/\partial z$ is the vertical shear of the tangential velocity. The authors argue that a necessary condition for the formation of the UIL is that $A(t) < 0$ in the upper troposphere. Since the vortex is approximately in thermal wind balance in the interior of the vortex, the two terms in A nearly cancel in the interior. According to their argument, the needed sign change of A comes about primarily when the radial temperature gradient term becomes negative in the lower stratosphere. They identified three candidate mechanisms in the lower stratosphere that would produce such a negative temperature gradient: an outer-core cold annulus; an inner-core warm ring; or “the evaporation or vertical diffusion of clouds at both the eyewall and inner edge and on top of the cloud overcast”, which would, according to the authors, “induce some penetrative downdrafts and further strengthen the UIL”. Unfortunately, this explanation is difficult to understand since it relies primarily on thermodynamics and does not account for the net radial force imbalance that would be required to generate an inflow just above a strong outflow layer. Moreover, the argument invokes hydrostatic dynamics and only provides a necessary condition in this framework, requiring the net time integral of the thermal wind residual to change sign. Finally, it is unclear whether this argument would have validity in an explanation of an upper-level inflow layer that is below the primary outflow layer.

APPENDIX B. DETERMINATION OF THE VORTEX CENTRE

The determination of the minimum wind, which is used as the centre location for carrying out an azimuthal average, is as follows. First, the wind field at the surface is smoothed by applying a 1-2-1 filter in the zonal and meridional direction 60 times. Then, the minimum wind speed and its location are determined in the smoothed wind field in a 60 km × 60 km box centred on the domain centre.

For horizontal cross-sections, the minimum wind used to define the centre is calculated in the same way, but at each particular height separately.

At an early stage of the study, we examined an alternative possibility to define the vortex centre as the location of minimum pressure in a similarly smoothed pressure field. Most of the time, the location of minimum pressure and minimum wind speed are close to each other below the outflow layer, but in the upper troposphere, the minimum pressure centre sometimes has a larger displacement: for example, at 74 hr, the horizontal displacement of the min-

imum pressure between 14 km and the surface is a little more than 1 km, but there is no displacement when centre location is based on the minimum wind speed. At earlier stages of development, such as 42 hr, the horizontal displacement of the minimum pressure between 14 km and the surface is 50 km, while for minimum wind centre it is only 13 km. For this reason, the minimum wind centre is preferred here.